

REVIEW ARTICLE

Quantum transport in topological semimetals under magnetic fields (II)

Hai-Peng Sun^{1,2,3}, Hai-Zhou Lu^{2,3,†}

¹Department of Physics, Harbin Institute of Technology, Harbin 150001, China

²Shenzhen Institute for Quantum Science and Engineering and Department of Physics, Southern University of Science and Technology, Shenzhen 518055, China

³Shenzhen Key Laboratory of Quantum Science and Engineering, Shenzhen 518055, China

Corresponding author. E-mail: [†]luhz@sustc.edu.cn

Received December 18, 2018; accepted February 28, 2019

We review our recent works on the quantum transport, mainly in topological semimetals and also in topological insulators, organized according to the strength of the magnetic field. At weak magnetic fields, we explain the negative magnetoresistance in topological semimetals and topological insulators by using the semiclassical equations of motion with the nontrivial Berry curvature. We show that the negative magnetoresistance can exist without the chiral anomaly. At strong magnetic fields, we establish theories for the quantum oscillations in topological Weyl, Dirac, and nodal-line semimetals. We propose a new mechanism of 3D quantum Hall effect, via the “wormhole” tunneling through the Weyl orbit formed by the Fermi arcs and Weyl nodes in topological semimetals. In the quantum limit at extremely strong magnetic fields, we find that an unexpected Hall resistance reversal can be understood in terms of the Weyl fermion annihilation. Additionally, in parallel magnetic fields, longitudinal resistance dips in the quantum limit can serve as signatures for topological insulators.

Keywords topological semimetal, topological insulator, quantum oscillation, negative magnetoresistance, quantum Hall effect

Contents	
1	Introduction
2	Models for topological semimetals and insulators
2.1	Topological Weyl semimetal
2.2	Topological Dirac semimetal
2.3	Topological nodal-line semimetal
2.4	Topological insulator
3	Weak field: Negative magnetoresistance in topological insulators
3.1	Anomalous velocity
3.2	Magnetoresistance formula
3.3	Comparison with negative magnetoresistance in experiments
3.4	Discussions
4	Strong field: Quantum oscillation in Weyl and Dirac semimetals
4.1	Quantum oscillation in linear and parabolic limits of a Weyl semimetal
4.2	Resistivity peaks and integer Landau indices
4.3	Anomalous phase shift near the Lifshitz point of Weyl and Dirac semimetals
5	Strong field: Quantum oscillation in nodal-line semimetals
5.1	Phase shifts of nodal-line semimetals
5.2	Magnetoresistivity of nodal-line semimetals
5.3	Discussions
6	Strong field: 3D quantum Hall effect
6.1	Wormhole tunneling via Fermi arcs and Weyl nodes
6.2	Quantized Hall conductance
6.3	3D distribution of the edge states
6.4	Topological Dirac semimetals
7	Extremely strong field: Weyl fermion annihilation
7.1	Calculation of Landau bands with magnetic fields in the $x-z$ plane
7.2	Landau bands in the z -direction magnetic field
7.3	Landau bands in the x -direction magnetic field
8	Extremely strong field: Forbidden backscattering and resistance dip in the quantum limit
8.1	Forbidden backscattering in the quantum limit
8.2	Conductivity in the quantum limit

*Special Topic: Recent Advances in Topological Materials (Eds. Yugui Yao, Xiangang Wan, Shengyuan A. Yang & Hua Chen). arXiv: 1812.10120.

9	Remarks and perspective	14
	Acknowledgements	15
	References	15

1 Introduction

In the previous article, we have reviewed our recent works on quantum transport phenomena in topological Weyl and Dirac semimetals under magnetic fields [1], which covers weak (anti-)localization [2, 3], negative magnetoresistance in Weyl/Dirac semimetals [4], and magnetotransport in the quantum limit [5, 6]. In this review, we summarize our recent works that were not addressed in Ref. [1], specifically, on the 3D quantum Hall effect [7], quantum oscillations in Weyl/Dirac [8] and nodal-line semimetals [9], and negative magnetoresistance in topological insulators [10], Weyl-node annihilation, [11] and vanishing backscattering [12] in the quantum limit. Following the structure in the previous review, these phenomena are organized depending on the strength of the magnetic field. There are several recent review papers on topological semimetals [13–16].

The structure of this review is as the following. In Section 2, we introduce the models we used for describing Weyl, Dirac, nodal-line semimetals, and topological insulators. In Section 3, we survey the negative magnetoresistance without chiral anomaly in topological insulators [10]. In Section 4, we discuss quantum oscillations with the anomalous phase shift in topological semimetals [8]. In Section 5, we present the rules for phase shifts of quantum oscillations in topological nodal-line semimetals [9]. In Section 6, we predict a 3D quantum Hall effect of Fermi arcs in topological semimetals [7]. In Section 7, we present the theory for the Weyl fermion annihilation in the quantum limit. The signature is recently observed as a sharp reversal in the Hall resistance of the topological Weyl semimetal TaP at extremely strong magnetic fields [11]. In Section 8, we propose that resistance dips in the quantum limit can serve as a signature for topological insulators because of forbidden backscattering [12]. Finally, we remark on future works in Section 9.

2 Models for topological semimetals and insulators

In this section, we introduce the models we used for describing Weyl, Dirac, nodal-line semimetals, and topological insulators.

2.1 Topological Weyl semimetal

The topological Weyl and Dirac semimetal are 3D topological states of matter [17–28]. Their energy bands touch at the Weyl nodes which host monopoles. The Weyl nodes have been verified in the Dirac semimetals Na₃Bi

[24, 29, 30] and Cd₃As₂ [4, 26, 31–36], and the Weyl semimetal TaAs family [37–43, 43–52], TaIrTe₄ [53] and YbMnBi₂ [54]. Also, Weyl semimetals can be induced from half-Heusler compounds by applying magnetic fields [55–57].

According to Section 2.1 of Ref. [1], a Weyl semimetal can be described by a two-node Hamiltonian [58–60]

$$H = A(k_x \sigma_x + k_y \sigma_y) + M(k_w^2 - \mathbf{k}^2) \sigma_z, \quad (1)$$

where $(\sigma_x, \sigma_y, \sigma_z)$ are the Pauli matrices, $\mathbf{k} = (k_x, k_y, k_z)$ is the wave vector, A , M , and k_w are model parameters. The eigen energies of the Hamiltonian are $E_{\pm}^{\mathbf{k}} = \pm[M^2(k_w^2 - \mathbf{k}^2)^2 + A^2(k_x^2 + k_y^2)]^{1/2}$, with $+$ for the conduction band and $-$ for the valence band. The two Weyl nodes are at $(0, 0, \pm k_w)$, and it has been demonstrated that the model is of all the topological semimetal properties [60], in particular, the Fermi arcs [6], different from the $k \cdot \sigma$ model [2, 61, 62]. This model has the topological properties because of the σ_z term [63]. For the 3D quantum Hall effect in Section 6, the above model is added with two trivial D terms [58–60]

$$H = D_1 k_y^2 + D_2(k_x^2 + k_z^2) + A(k_x \sigma_x + k_y \sigma_y) + M(k_w^2 - \mathbf{k}^2) \sigma_z. \quad (2)$$

2.2 Topological Dirac semimetal

A Dirac semimetal can be regarded as a Weyl semimetal and its time-reversal partner. Dirac semimetals can be studied by using the Hamiltonian [24, 26, 64]

$$H = \varepsilon_0(\mathbf{k}) + \begin{pmatrix} M(\mathbf{k}) & Ak_+ & 0 & 0 \\ Ak_- & -M(\mathbf{k}) & 0 & 0 \\ 0 & 0 & M(\mathbf{k}) & -Ak_- \\ 0 & 0 & -Ak_+ & -M(\mathbf{k}) \end{pmatrix} + \frac{\mu_B}{2} (\boldsymbol{\sigma} \cdot \mathbf{B}) \otimes \begin{pmatrix} g_s & 0 \\ 0 & g_p \end{pmatrix}, \quad (3)$$

where g_s is the g factor for the s band, g_p is the g factor for the p band [64], $k_{\pm} = k_x \pm ik_y$, $\varepsilon_0(\mathbf{k}) = C_0 + C_1 k_z^2 + C_2(k_x^2 + k_y^2)$, and $M(\mathbf{k}) = M_0 + M_1 k_z^2 + M_2(k_x^2 + k_y^2)$. The x , y , and z axes in the Hamiltonian are defined along the [100], [010], and [001] crystallographic directions, respectively.

2.3 Topological nodal-line semimetal

Nodal-line semimetals [65–68], in which the cross sections of conduction and valence bands are closed rings [Fig. 3(a)] in momentum space [69–72], have the drumhead surface states, of which the direct evidence is still missing [73]. Recently, a new type of surface state called the floating band was discovered in the nodal-line semimetal Zr-SiSe [74]. Besides, when the symmetries are broken, the nodal-line semimetals may develop into Dirac semimetals, topological insulators, and surface Chern insula-

tors [75]. The nodal lines are predicted in many materials, such as HgCr_2Se_4 [20], graphene networks [76], $\text{Cu}_3(\text{Pd/Zn})\text{N}$ [77, 78], SrIrO_3 [79, 80], TlTaSe_2 [81], Ca_3P_2 [82, 83], CaTe [84], compressed black phosphorus [85], CaAg(P/As) [86], CaP_3 family [87], PdS monolayer [88], Zintl compounds [89], BaMX_3 ($M = \text{V}, \text{Nb}$ and Ta , $X = \text{S}, \text{Se}$) [90], rare earth monopnictides [91], alkaline-earth compounds [92–94], other carbon-based materials [69, 95], and metallic rutile oxides $X\text{O}_2$ ($X = \text{Ir}, \text{Os}, \text{Rd}$) [96]. So far, the nodal lines have been verified in ZrSiS [97–99], PbTaSe_2 [100, 101], InBi [102] and PtSn_4 [103] by ARPES.

The Hamiltonian of nodal-line semimetals can be described as [81, 100]

$$H = \left\{ [\hbar^2(k_x^2 + k_y^2)/(2m) - u] \tau_3 + \lambda k_z \tau_1 \right\} \otimes \sigma_0, \quad (4)$$

where $\mathbf{k} = (k_x, k_y, k_z)$ is the wave vector, τ, σ are the Pauli matrices, λ, m , and u are model parameters [81, 100]. The eigen energies of the Hamiltonian are $E_{\pm} = \pm \sqrt{[\hbar^2(k_x^2 + k_y^2)/(2m) - u]^2 + \lambda^2 k_z^2}$. When u is positive, two bands intersect at zero energy as $k_x^2 + k_y^2 = 2mu/\hbar^2$, which describes the nodal-line ring. The radius of the nodal ring is $\sqrt{2mu}/\hbar$ [Fig. 3(a)]. When $E_F < u$, the dispersions result in a torus Fermi surface [Fig. 3(a)]. When $E_F > u$, the Fermi surface evolves into a drum-like structure [Fig. 3(a)]. Because of the low carrier density of the samples in experiments [97, 98], we focus on the case that $E_F < u$. Moreover, the model in Eq. (4) is of the mirror reflection symmetry [81, 100]. Nodal lines can also be protected by other symmetries [67, 70, 78, 104], for example, two-fold screw rotation [79, 80], four-fold rotation, inversion [67] and non-symmorphic symmetry through a glide plane [97, 98], etc.

2.4 Topological insulator

3D topological insulators can be described by the $\mathbf{k} \cdot \mathbf{p}$ Hamiltonian [58, 105, 106]

$$H_0 = C_{\mathbf{k}} + \begin{pmatrix} M_{\mathbf{k}} & 0 & iV_n k_z & -iV_{\perp} k_- \\ 0 & M_{\mathbf{k}} & iV_{\perp} k_+ & iV_n k_z \\ -iV_n k_z & -iV_{\perp} k_- & -M_{\mathbf{k}} & 0 \\ iV_{\perp} k_+ & -iV_n k_z & 0 & -M_{\mathbf{k}} \end{pmatrix}, \quad (5)$$

where $M_{\mathbf{k}} = M_0 + M_{\perp}(k_x^2 + k_y^2) + M_z k_z^2$, $C_{\mathbf{k}} = C_0 + C_{\perp}(k_x^2 + k_y^2) + C_z k_z^2$, C_i, M_i and V_i are model parameters. The model depicts a 3D strong topological insulator as $M_0 M_{\perp} < 0$ and $M_0 M_z < 0$ [58]. There are four energy bands $\varepsilon_n(\mathbf{k})$ near the Γ point, two conduction bands and two valence bands (see Fig. 2 in Ref. [10]). The model has been shown effective to give proper descriptions for the topological surface states [63, 107, 108] and explain the negative magnetoresistance in topological insulators [10, 109–112].

In the presence of the magnetic field, the Zeeman Hamiltonian reads

$$H_Z = \frac{\mu_B}{2} \begin{pmatrix} g_z^v B_z & g_p^v B_- & 0 & 0 \\ g_p^v B_+ & -g_z^v B_z & 0 & 0 \\ 0 & 0 & g_z^c B_z & g_p^c B_- \\ 0 & 0 & g_p^c B_+ & -g_z^c B_z \end{pmatrix}, \quad (6)$$

where $g_{v/c,z/p}$ are Landé g -factors for valence/conduction bands along the z direction and in the $x-y$ plane and μ_B is the Bohr magneton.

3 Weak field: Negative magnetoresistance in topological insulators

Recently discovered topological semimetals can host the chiral anomaly, namely, the violation of the conservation of chiral current [113–115], which is widely believed to be the cause of the negative magnetoresistance [4, 35, 36, 45, 46, 116–123]. Nevertheless, in topological insulators, where the chiral anomaly is not well defined in the momentum space, a negative magnetoresistance can also be observed. This results in great confusion [109–112, 124–126] on the explanation of the negative magnetoresistance. Lately, it is found that the chiral anomaly in real space can be defined in a quantum spin Hall insulator [127]. In Ref. [10], we use the semiclassical Boltzmann formalism with the Berry curvature and orbital moment, to explain the negative magnetoresistance in topological insulators, and show a quantitative agreement with the experiments (see Fig. 1).

3.1 Anomalous velocity

The Berry curvature and orbital moment will induce the anomalous velocity, which may lead to the negative magnetoresistance. In experiments, the negative magnetoresistance exists above $T = 100$ K [111], thus quantum interference mechanisms can be excluded. In addition, due to the poor mobility in the topological insulators Bi_2Te_3 and Bi_2Se_3 [129], when the magnetic field is up to 6 Tesla, the Landau levels cannot be well-formed. In the semiclassical regime, the electronic transport can be described by the equations of motion [130]

$$\dot{\mathbf{r}} = \frac{1}{\hbar} \nabla_{\mathbf{k}} \tilde{\varepsilon}_{\mathbf{k}} - \dot{\mathbf{k}} \times \Omega_{\mathbf{k}}, \quad \dot{\mathbf{k}} = -\frac{e}{\hbar} (\mathbf{E} + \dot{\mathbf{r}} \times \mathbf{B}), \quad (7)$$

where both the position \mathbf{r} and wave vector \mathbf{k} appear simultaneously, $\dot{\mathbf{r}}$ and $\dot{\mathbf{k}}$ are their time derivatives, $-e$ is the electron charge, \mathbf{E} and \mathbf{B} are external electric and magnetic fields, respectively. $\tilde{\varepsilon}_{\mathbf{k}} = \varepsilon_{\mathbf{k}} - \mathbf{m} \cdot \mathbf{B}$, $\varepsilon_{\mathbf{k}}$ is the band dispersion, \mathbf{m} is the orbital moment induced by the semiclassical self-rotation of the Bloch wave packet, and $\Omega_{\mathbf{k}}$ is the Berry curvature [131]. In the linear-response limit ($\mathbf{E} = 0$), Eq. (7) yields an effective velocity

$$\dot{\mathbf{r}} = [\tilde{\mathbf{v}}_{\mathbf{k}} + (e/\hbar) \mathbf{B} (\tilde{\mathbf{v}}_{\mathbf{k}} \cdot \Omega_{\mathbf{k}})] / D_{\mathbf{k}}, \quad (8)$$

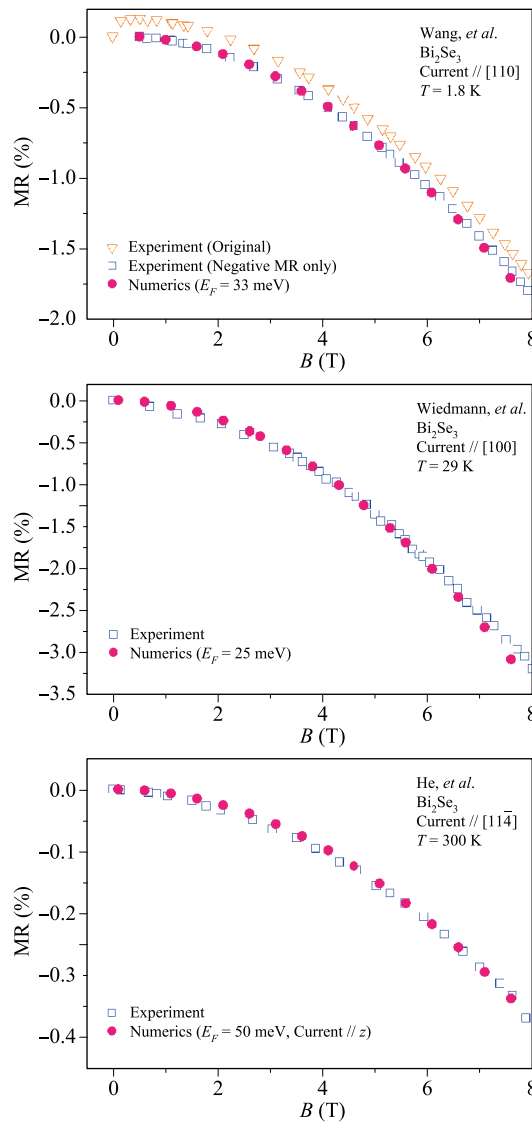


Fig. 1 The comparison between the calculated negative magnetoresistance [10] and the experiments [109–111]. The Fermi energy E_F is measured from the conduction band bottom. E_F falls in a reasonable range. x, y, z in the model (5) correspond to [100], [010], and [001] crystallographic directions, respectively. The numerically calculated magnetoresistance along the z axis is used to approach the experimental magnetoresistance along the [11̄] direction by He *et al.*. Other model parameters are from the $k\cdot p$ calculations [106] and experiments [128], $M_0 = -0.169$ eV, $M_z = 3.351$ eV·Å 2 , $M_{\perp} = 29.36$ eV·Å 2 , $V_{\perp} = 2.512$ eV·Å, $V_n = 1.853$ eV·Å, $C_0 = 0.048$ eV, $C_z = 1.409$ eV·Å 2 , $C_{\perp} = 13.9$ eV·Å 2 , the g -factors $g_v^z = g_z^c = 30$ and $g_v^y = g_p^c = -20$. Reproduced from Ref. [10].

where $D_{\mathbf{k}}^{-1}$ is the correction to the density of states, and

$$\tilde{\mathbf{v}}_{\mathbf{k}} = \mathbf{v}_{\mathbf{k}} - \frac{1}{\hbar} \nabla_{\mathbf{k}} (\mathbf{m}_{\mathbf{k}} \cdot \mathbf{B}), \quad D_{\mathbf{k}} = 1 + \frac{e}{\hbar} \mathbf{B} \cdot \boldsymbol{\Omega}_{\mathbf{k}}. \quad (9)$$

Due to the Berry curvature, the velocity develops an anomalous term, which is proportional to \mathbf{B} . Note that the conductivity is the current-current (velocity-velocity)

correlation [132], thus the presence of the anomalous velocity is expected to generate an extra conductivity, which grows with the magnetic field, namely, a negative magnetoresistance. It has been implied that the negative magnetoresistance in topological semimetals is related to the Berry curvature [1, 133, 134]. In our previous review [1], we have shown that the Berry curvature [130] can lead to a conductivity correction that grows with magnetic field B ,

$$\delta\sigma(B) \propto \frac{B^2}{k_F^2} \propto \frac{B^2}{n^{2/3}}, \quad (10)$$

where k_F is the Fermi wave vector and the carrier density n is directly proportional to k_F^3 . This is an alternative understanding to the negative magnetoresistance induced by the chiral anomaly. Ref. [10] shows that this mechanism is large enough in topological insulators as those observed in the experiments, where the relative magnetoresistance can exceed -1% in a parallel magnetic field of several Tesla [109–112, 124–126].

3.2 Magnetoresistance formula

In our calculation, the relative magnetoresistance is defined as $\text{MR}_{\mu}(B_{\mu}) = [1/\sigma^{\mu\mu}(B_{\mu}) - 1/\sigma^{\mu\mu}(0)]/[1/\sigma^{\mu\mu}(0)]$. In the semiclassical Boltzmann formalism, the longitudinal conductivity $\sigma^{\mu\mu}$ is contributed by all the bands crossing the Fermi energy, and for band n [134]

$$\sigma^{\mu\mu} = \int \frac{d^3\mathbf{k}}{(2\pi)^3} \frac{e^2\tau}{D_{\mathbf{k}}} \left(\tilde{v}_{\mathbf{k}}^{\mu} + \frac{e}{\hbar} B^{\mu} \tilde{v}_{\mathbf{k}}^{\nu} \Omega_{\mathbf{k}}^{\nu} \right)^2 \left(-\frac{\partial \tilde{f}_0}{\partial \tilde{\varepsilon}} \right), \quad (11)$$

where n is suppressed for simplicity, $D_{\mathbf{k}}$ and $\tilde{v}_{\mathbf{k}}^{\mu}$ are given by Eq. (9), \tilde{f}_0 is the Fermi distribution in equilibrium, the transport time τ is assumed to be a constant in the semiclassical limit [135]. For the n -th band of the Hamiltonian H , the ξ component of the Berry curvature vector can be found as $\Omega_{n\mathbf{k}}^{\xi} = \Omega_{n\mathbf{k}}^{\mu\nu} \varepsilon_{\mu\nu\xi}$, where ξ, μ, ν stand for x, y, z , and $\varepsilon_{\mu\nu\xi}$ is the Levi-Civita anti-symmetric tensor, and

$$\Omega_{n\mathbf{k}}^{\mu\nu} = -2 \sum_{n' \neq n} \frac{\text{Im}\langle n | \partial H / \partial k_{\mu} | n' \rangle \langle n' | \partial H / \partial k_{\nu} | n \rangle}{(\varepsilon_n - \varepsilon'_n)^2}, \quad (12)$$

where $H = H_0 + H_Z$. The orbital moment \mathbf{m} can be found as

$$m_{n\mathbf{k}}^{\mu\nu} = -\frac{e}{\hbar} \sum_{n' \neq n} \frac{\text{Im}\langle n | \partial H / \partial k_{\mu} | n' \rangle \langle n' | \partial H / \partial k_{\nu} | n \rangle}{\varepsilon_n - \varepsilon'_n}. \quad (13)$$

The Zeeman energy can induce a finite distribution of Ω and \mathbf{m} [10].

3.3 Comparison with negative magnetoresistance in experiments

Figure 1 shows that the numerically calculated relative magnetoresistance in parallel magnetic fields are negative

and decrease monotonically with the magnetic field. They can be fitted by $-B^2$ at small magnetic fields and conform to the Onsager reciprocity $\text{MR}(B) = \text{MR}(-B)$. We also use a tight-binding model [136] to justify the calculation. Figure 1 shows a good agreement on the negative magnetoresistance between the experiments and our numerical calculations. The current direction and temperature are from the experiments and the model parameters are from the $k \cdot p$ calculations [106] and experiments [128]. In the experiment by Wang *et al.* [109], the temperature is 1.8 K, so the original data (orange triangles) has a positive magnetoresistance near zero field due to the weak anti-localization [137–140]. The weak anti-localization induces a positive magnetoresistance [2], which is subtracted before the comparison. In the experiments by Wiedmann *et al.* [111] and He *et al.* [110], the temperatures are 29 K and 300 K, there is no weak anti-localization effect. The negative magnetoresistance does not change much with temperature [10], consistent with the experiments and showing the semi-classical nature of the negative magnetoresistance. The negative magnetoresistance becomes enhanced as the Fermi level approaches the band bottom [10], indicating the role of the Berry curvature. Ref. [10] also shows that the signs of g -factors in the Zeeman coupling determine the signs of magnetoresistance qualitatively. In the experiment, the techniques used for topological insulators, for example, electron spin resonance and quantum oscillations, cannot determine the signs of g -factors but only their absolute values [128, 141]. Transport measurements can determine the sign of the g -factor only in specific setups [142]. The orbital moment has been neglected in most of the literature studying the magneto-transport using the semiclassical formalism [133, 134]. As shown in Refs. [143, 144], the orbital moment is essential for the magnetoresistance anisotropy in a Weyl semimetal. Moreover, the correction $\mathbf{m} \cdot \mathbf{B}$ to $\varepsilon(\mathbf{k})$ can enhance the band separation and the negative magnetoresistance. The orbital moment effectively enhances the MR_x a few times larger. MR_z can be even positive without \mathbf{m} .

3.4 Discussions

The conventional equations of motion in the low-field semiclassical regime ($\omega\tau \ll 1$) are only accurate to the linear order in the external fields (\mathbf{E} and \mathbf{B}), thus for studying magnetoconductivity which is an intrinsically nonlinear coefficient, the obtained results would not be complete. Based on a recently developed semiclassical theory with second-order accuracy [145, 146], a complete theory of magnetoconductivity for general 3D nonmagnetic metals was formulated within the Boltzmann framework with the relaxation time approximation [144]. The work shows several surprising results. First, there is an important previously unknown Fermi surface contribution $\delta\sigma^{\text{int}}$ to the magnetoconductivity, termed as the intrinsic magnetoconductivity, because the ratio $\delta\sigma^{\text{int}}/\sigma_0$ is independent of the relaxation time. Here σ_0 is the conductivity

at $B = 0$. Second, a pronounced $\delta\sigma^{\text{int}}$ term can lead to the violation of Kohler's rule. Previously, any deviation from Kohler's rule is usually interpreted as from factors beyond the semiclassical description or from the presence of multiple types of carriers or multiple scattering times. The result here reveals a new mechanism for the breakdown of Kohler's rule. Third, $\delta\sigma^{\text{int}}$ can lead to a positive longitudinal magnetoconductivity (or negative longitudinal magneto-resistivity). The effect is independent of chiral anomaly effect for the Weyl/Dirac fermions, and it can occur for a generic doped semiconductor without any band crossings. This indicates that positive longitudinal magnetoconductivity measured in the semiclassical regime alone cannot be regarded as smoking-gun evidence for the existence of topological band crossings. The intrinsic contribution generally exists in 3D metals with nontrivial Berry curvatures, and should be taken into account when interpreting experimental results. It may already play an important role behind the puzzling magnetotransport signals observed in recent experiments on TaAs₂ and related materials.

In the quantum limit where only the lowest Landau band is occupied, magnetoresistance depends subtly on scattering mechanisms [5, 6, 147], rather than the Berry curvature and orbital moment. The current-jetting effect is usually induced by inhomogeneous currents when attaching point contact electrodes to a large bulk crystal and may also hamper the interpretation of the negative magnetoresistance data [148]. A recent work also has pointed out that the negative magnetoresistance may exist without the chiral anomaly [149]. In (Bi_{1-x}In_x)₂Se₃, it is proposed that the in-plane negative magnetoresistance is due to the topological phase transition enhanced intersurface coupling near the topological critical point [126]. In addition, it is also found that the magnetoresistance is robust against the deviation from the ideal Weyl Hamiltonian, such as the shifted Fermi energy, nonlinear dispersions, and the Weyl node annihilation [150].

4 Strong field: Quantum oscillation in Weyl and Dirac semimetals

When applying a magnetic field in the z -direction, the energy spectrum evolves into a series of 1D Landau bands [6, 60] (see Figs. 1(b) and (c) of [8]), which result in the Shubnikov-de Haas (SdH) oscillation of resistance. The oscillation of the resistivity ρ can be demonstrated by the Lifshitz-Kosevich formula [151]

$$\rho \sim \cos[2\pi(F/B + \phi)], \quad (14)$$

where ϕ is the phase shift, F is the oscillation frequency and B is the magnitude of magnetic field. F and ϕ can reveal valuable details on the Fermi surface of the material.

The phase shift of each frequency component can be

argued as the following:

$$\phi = -1/2 + \phi_B/(2\pi) + \phi_{3D}, \quad (15)$$

where $\phi_{3D} = \mp 1/8$ is a correction, which emerges only in 3D, and ϕ_B is the Berry phase [131, 152]. The curvature of the Fermi surface along the direction of the magnetic field determines the sign of ϕ_{3D} [153–156]. When the cross section is maximum, for electron carriers $\phi_{3D} = -1/8$ and for hole carriers $\phi_{3D} = 1/8$; when the cross section is minimum, for electron carriers $\phi_{3D} = 1/8$ and for hole carriers $\phi_{3D} = -1/8$. For the sphere Fermi surface, there is only a maximum, thus for electron carriers $\phi_{3D} = -1/8$ and for hole carriers $\phi_{3D} = 1/8$. For a parabolic energy band, it does not have Berry phase, thus the phase shift is $\pm 1/2$ and $\pm 5/8$ in 2D and 3D, respectively. However, a linear energy band (for example, Weyl and Dirac semimetals [17–20, 157]) has an extra π Berry phase [152], thus the phase shift is 0 [158] and $\pm 1/8$ [159] in 2D and 3D, respectively. In a nodal-line semimetal [65–68], an electron can collect a nontrivial π Berry phase around the loop encircling the nodal line [79]. The phase shifts of 2D and 3D bands with linear and parabolic dispersions are summarized in Table 1.

Topological Weyl/Dirac semimetals and nodal-line semimetals provide a novel platform to explore the nontrivial Berry phase [3, 119, 122, 159–175]. In Ref. [8], we show that, near the Lifshitz point, the phase shift of the quantum oscillation can go beyond recognized values of $\pm 1/8$ or $\pm 5/8$ and nonmonotonically move toward a wide range between $\pm 7/8$ and $\pm 9/8$. However, these values in experiments may be misunderstood as $\pm 1/8$. For Dirac semimetals, the total phase shift adopts the discrete values of $\pm 1/8$ or $\pm 5/8$. In recent experiments of electron carriers, the positive phase shifts are observed and may be explained by our findings. In addition, a new beating pattern, resulting from the topological band inversion, is found. Up to now, quantum oscillations have been inspected experimentally in HfSiS [176], ZrSiS [177–182], ZrSi(Se/Te) [183] and ZrGe(S/Se/Te) [184], but the phase shifts have been concluded different. In Ref. [9], the phase shifts and frequencies (Table 5) of nodal-line semimetals

Table 1 Phase shifts ϕ in Eq. (14) for systems with different dispersions (linear or parabolic) and dimensionalities (2D or 3D). B_z and B_{\parallel} are the magnetic fields out of and in the nodal-line plane. α , β , γ , and δ correspond to the cross sections of the torus Fermi surface in Fig. 3. Reproduced from Ref. [9].

System	Electron carrier	Hole carrier
2D parabolic	-1/2	1/2
3D parabolic	-5/8	5/8
2D linear	0	0
3D linear	-1/8	1/8
Nodal-line in B_z	-5/8 (α), 5/8 (β)	5/8 (α), -5/8 (β)
Nodal-line in B_{\parallel}	-5/8 (γ), 1/8 (δ)	5/8 (γ), -1/8 (δ)

are extracted from analytic results of the calculated resistivity. We also summarize the generic rules for phase shifts in random cases (Table 4). The generic rules assist us to handle several materials, for example, ZrSiS and Cu₃PdN [177–182].

4.1 Quantum oscillation in linear and parabolic limits of a Weyl semimetal

The resistivity is calculated in two direction configurations according to linear response theory [185–188]. For the longitudinal configuration, the resistivity ρ_{zz} is examined along z direction. For the transverse configuration, the resistivity ρ_{xx} is examined along x direction. The magnetoresistivity in the linear dispersion limit and parabolic dispersion limit takes the form of Eq. (14). In Table 2, we list the analytic expressions for the phase shift ϕ and frequency F in these two limits.

4.2 Resistivity peaks and integer Landau indices

In the experiment, the peak positions or valley positions, that are on the B axis, are given the integer Landau indices n , then the phase shift ϕ and frequency F can be extracted from a plot of n and $1/B$ [see inset of Fig. 1(d) of [8]]. Nevertheless, it is still in debate that whether the peaks [122, 159, 160, 162–165] or valleys [167, 168, 171, 189] should be given the Landau indices. Our results explicitly reveal that the resistivity peaks of ρ_{zz} and ρ_{xx} emerge near the Landau band edges and are in correspondence with the integer Landau indices. We evaluate the resistivity components theoretically from the conductivity components [190, 191]. For the longitudinal configuration, the resistivity $\rho_{zz} = 1/\sigma_{zz}$, where the conductivity σ_{zz} is along z direction. Near band edges, the conductivity σ_{zz} shows valleys due to vanishing velocities, thus ρ_{zz} shows peaks. For the transverse configuration, $\rho_{xx} = \sigma_{yy}/(\sigma_{yy}^2 + \sigma_{xy}^2)$, and the longitudinal Hall conductivity and field-induced Hall conductivity are as follows:

$$\sigma_{yy} = \frac{\sigma_0(1+\delta)}{1+(\mu B)^2}, \quad \sigma_{yx} = \frac{\mu B \sigma_0}{1+(\mu B)^2} \left[1 - \frac{\delta}{(\mu B)^2} \right], \quad (16)$$

where $\delta \ll 1$ is the oscillation part and σ_0 represents the zero-field conductivity. In σ_{yx} , the δ term, which comes

Table 2 The analytical expressions for the frequency F and phase shift ϕ in the resistivity formula Eq. (14) in the linear and parabolic dispersion limits for electron carriers in a Weyl semimetal. We define $E'_F \equiv E_F + M k_w^2$. Reproduced from Ref. [8].

	Longitudinal ρ_{zz}		Transverse ρ_{xx}	
	Parabolic	Linear	Parabolic	Linear
F	$\hbar E'_F/(2eM)$	$\hbar E_F^2/(2eA^2)$	$\hbar E'_F/(2eM)$	$\hbar E_F^2/(2eA^2)$
ϕ	-5/8	-1/8	-5/8	-1/8

from the disorder scattering, was rarely considered before. A consequence of the δ term is that $\rho_{xx} \approx (1+\delta)/\sigma_0$, up to the first order of δ . As ρ_{xx} and σ_{yy} are both proportional to $1+\delta$, their peaks are lined up for the random ratio of σ_{yx} to σ_{yy} (but when $\sigma_{yx} \ll \sigma_{yy}$, the oscillation is so weak that it is hard to be observed). This new finding comes from the disorder scattering term δ in the Hall conductance. At the same time, the σ_{zz} valleys are lined up with the σ_{yy} peaks, since σ_{zz} , which comes from diffusion, is in proportion to the scattering times. However, σ_{yy} , which arises from hopping is inversely in proportion to the scattering times [60, 186, 192]. To sum up, the peak positions follow the relation $\rho_{zz} \sim \sigma_{zz}^{-1} \sim \sigma_{yy} \sim \rho_{xx}$, thus ρ_{zz} and ρ_{xx} present peaks near Landau band edges and their phase shifts are the same.

4.3 Anomalous phase shift near the Lifshitz point of Weyl and Dirac semimetals

Figure 2 shows the results of the frequency F and the phase shift ϕ calculated numerically for the model in Eq. (1). In Fig. 2(c), the numerical results are in agreement with the analytical prediction $\phi = -1/8$ for the linear limit ($E_F \rightarrow 0$) and $-5/8$ for the parabolic limit ($E_F \rightarrow \infty$). We define $E_A = Ak_w$ and $E_M = Mk_w^2$. For $E_M \neq E_A$, the ϕ - E_F curves break as the beating patterns emerge. In Fig. 2(c), for $E_A < E_M$, the phase shift drops below $-5/8$ rather than shift monotonically from $-1/8$ to $-5/8$ around the Lifshitz transition point (namely, $E_F = E_M$). This is because there is no simple k_z^2 dependence [8]. At the Lifshitz point, we can analytically show that the phase shift is $-9/8$, which is in agreement with that in Fig. 2(c). It is equivalent to $-1/8$, which is usually considered to originate from the π Berry phase as the Fermi sphere encircles the single Weyl node. Nevertheless, the Fermi sphere encircles two Weyl nodes when the Fermi energy is at the Lifshitz point. For $E_A > E_M$, there is no nonmonotonicity in $\phi - E_F$.

A Weyl semimetal combine with its time-reversal counterpart can compose a Dirac semimetal. The model of a Dirac semimetal can be made by $H(\mathbf{k})$ in Eq. (1), integrated with its time-reversal counterpart $H^*(-\mathbf{k})$, where the asterisk indicates complex conjugate. This model can be treated as a building block for Weyl semimetals, which respect time-reversal symmetry and meanwhile break inversion symmetry [37–39, 42–48]. Here, for the Dirac semimetal, the total phase shift may take two values, $-1/8$ for $\alpha \in [0, 1/4]$ and $[3/4, 1]$ or $-5/8$ for $\alpha \in [1/4, 3/4]$. Around the Lifshitz point, the total phase shift may change between the two values.

The electron carriers is supposed to yield negative phase shifts and the hole carriers is supposed to yield positive phase shifts [159]. Nevertheless, in experiments of the Dirac semimetal Cd₃As₂, the phase shift for electron carriers takes positive values [160, 162, 167]. One explanation may be that, for the phase shift 1/8 to 3/8 in the experiments, their actual values are around $-7/8$ to $-5/8$ due

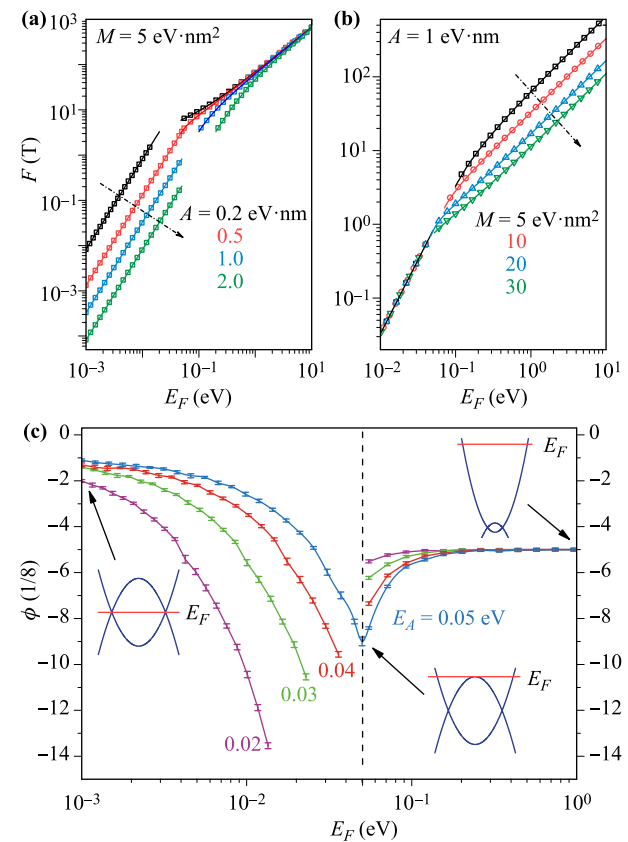


Fig. 2 For the Weyl semimetal described by Eq. (1). (a) The frequency F obtained numerically (scatters) and analytically (solid curves) vs. the Fermi energy E_F for (a) different A at a fixed M ; and (b) for different M at a fixed A . (c) The phase shift ϕ vs. E_F for different $E_A = Ak_w$ and a fixed $E_M = Mk_w^2 = 0.05$ eV. The curves break because F and ϕ cannot be fitted when beating patterns form. The insets indicate the location of Fermi energy. The vertical dashed lines mark the Lifshitz point. $k_w = 0.1$ nm⁻¹. Reproduced from Ref. [8].

Table 3 The phase shift ϕ_{exp} extracted from the experiments on Cd₃As₂. According to the theory in this work, if peaks from two Weyl components can be distinguished, the phase shift should be $\phi_{\text{Weyl}} = \phi_{\text{exp}} - 1$; otherwise, the phase shift should be $\phi_{\text{Dirac}} = -5/8$. Reproduced from Ref. [8].

Ref.	ϕ_{exp}	ϕ_{Weyl}	ϕ_{Dirac}
[160]	0.06–0.08	-0.94–-0.92	-5/8
[162]	0.11–0.38	-0.89–-0.62	-5/8
[167]	0.04 ¹⁾	-0.96	-5/8

¹⁾Read from Fig. 2(d) of Ref. [167].

to the 2π periodicity. Our numerical results show that the total phase shift adopts these values from around the Lifshitz point to higher Fermi energies, which is also consistent with the carrier density in the experiments. In Table 3, we propose the counterparts for the experimental values of the phase shift. In Ref. [8], we also demonstrate that beating patterns will emerge because of the band inversion, that is different from orbital quantum interfer-

ence [193], the Zeeman splitting [165, 166, 194] and nested Fermi surfaces [162].

5 Strong field: Quantum oscillation in nodal-line semimetals

5.1 Phase shifts of nodal-line semimetals

The frequencies F and phase shifts ϕ can be analyzed from the Fermi surface described by Eq. (4). From the Onsager relation, we have $F = [\hbar/(2\pi e)]A$, where A is the area of the extremal cross section on the Fermi surface perpendicular to the magnetic field [195]. When the nodal-line plane is perpendicular to a magnetic field, specifically B_z here, there are two extremal cross sections at the $k_z = 0$ plane [Fig. 3(b)]. Combining this dispersion with the Onsager relation, we find that the high frequency is $F_\alpha = m(u + E_F)/(\hbar e)$ for the outside circle and the low frequency is $F_\beta = m(u - E_F)/(\hbar e)$ for the inside circle. These two frequencies may lead to a beating pattern [196].

Phase shifts are more complicated in the nodal-line semimetals. First of all, whether the magnetic fields are in-plane or out-of-plane, the torus Fermi surface has both maximum cross section and minimum cross section. Secondly, the Berry phase is 0 along the circle parallel to the nodal line and is π along the circle enclosing the nodal line. Therefore, depending on direction of the magnetic

field, the quantum oscillation allows different phase shifts, which is summarized in Table 1. When the nodal-line plane is perpendicular to a magnetic field, there are two cross sections α and β , shown in Fig. 3. Along loops of the cross sections α and β , the Berry phase is 0, thus phase shifts take values $5/8$ or $-5/8$. For the electron carriers, (see Table 4), the phase shifts of the maximum cross section α are $\phi_{3D} = -1/8$ and $\phi = -1/2 + 0 - 1/8 = -5/8$. The phase shifts of the minimum cross section β are $\phi_{3D} = 1/8$ and $\phi = -1/2 + 0 + 1/8 = -3/8$, that is equivalent to $5/8$ since the oscillation has 2π periodicity.

5.2 Magnetoresistivity of nodal-line semimetals

To testify the above conclusion, we calculate the resistivities along the z (ρ_{zz} , out of the nodal-line plane) and x (ρ_{xx} , in the nodal-line plane) directions, respectively, according to $\rho_{zz} = 1/\sigma_{zz}$ and $\rho_{xx} = \sigma_{yy}/(\sigma_{yy}^2 + \sigma_{xy}^2)$. The calculations show that for both ρ_{xx} and ρ_{zz} , there are two terms in the magnetoresistivities,

$$(\rho - \rho_0)/\rho_0 = C_\alpha \exp(-\lambda_D) \cos[2\pi(F_\alpha/B + \phi_\alpha)] + C_\beta \exp(-\lambda_D) \cos[2\pi(F_\beta/B + \phi_\beta)], \quad (17)$$

where $\phi_{\alpha,\beta}$ is the phase shifts and $F_{\alpha,\beta}$ are the oscillation frequencies. Their analytic expressions are listed in Table 5. We show that the resistivity calculations and the Fermi surface analysis are equivalent for the phase shifts of the quantum oscillation in the nodal-line semimetal. The phase shifts, in a magnetic field parallel to the nodal-line plane [Fig. 3(c)], can also be found in a similar way, as listed in Table 4.

5.3 Discussions

For nodal-line semimetals, most of the quantum oscillation experiments have been done for the ZrSiS family materials [176–184], in which there are both electron and hole pockets at the Fermi energy [97, 98, 177, 182]. ZrSiS (see Fig. 3 in Ref. [9]) has the diamond-shaped electron pockets encircling the nodal line and the quasi-2D tubular-shaped

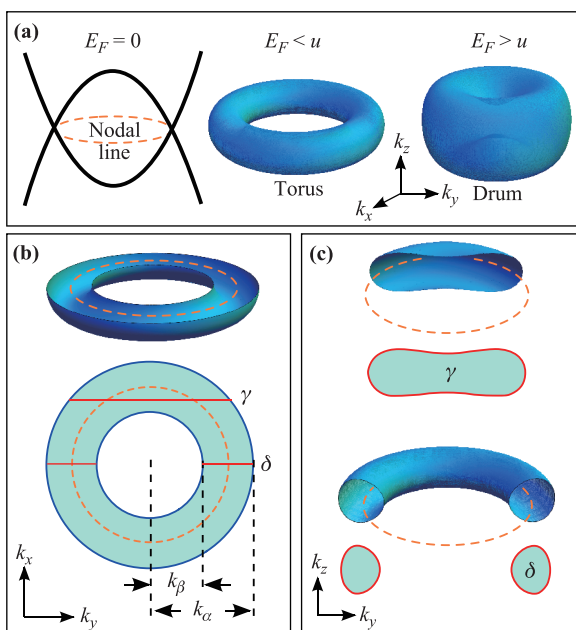


Fig. 3 (a) The nodal line (dashed ring), torus, and drum Fermi surfaces for a generic model of a nodal-line semimetal in Eq. (19). E_F is the Fermi energy. u is a model parameter. (b) The maximum (α) and minimum (β) cross sections in the nodal-line plane of the torus Fermi surface. (c) The maximum (γ) and minimum (δ) cross sections out of the nodal-line plane of the torus Fermi surface. Reproduced from Ref. [9].

Table 4 The phase shift ϕ of the nodal-line semimetal in Fig. 3, obtained by using the relation $\phi = -1/2 + \phi_B/(2\pi) + \phi_{3D}$, where ϕ_B is the Berry phase and ϕ_{3D} is the dimension correction. $\alpha, \beta, \gamma, \delta$ are the extremal cross sections in Fig. 3. Max. or Min. indicates whether the cross section is maximum or minimum. For electron carriers, ϕ_{3D} is $-1/8$ for maximum cross section and $1/8$ for minimum cross section. The phase shifts of hole carriers are opposite to those of electrons. Reproduced from Ref. [9].

	Berry phase	Min./max.	Electron	Hole
α	0	Max.	$-1/2 + 0 - 1/8 = -5/8$	$+5/8$
β	0	Min.	$-1/2 + 0 + 1/8 = -3/8 \leftrightarrow 5/8$	$-5/8$
γ	0	Max.	$-1/2 + 0 - 1/8 = -5/8$	$+5/8$
δ	π	Min.	$-1/2 + \pi/2\pi + 1/8 = 1/8$	$-1/8$

Table 5 The analytic expressions for the frequencies $F_{\alpha,\beta}$ and phase shifts $\phi_{\alpha,\beta}$ in the resistivity formula Eq. (17) for electron carriers. Hole carriers have an extra minus sign in all cases compared to electron carriers. Reproduced from Ref. [9].

Longitudinal ρ_{zz}		Transverse ρ_{xx}	
α	β	α	β
F	$\frac{m}{\hbar e}(u + E_F)$	$\frac{m}{\hbar e}(u - E_F)$	$\frac{m}{\hbar e}(u + E_F)$
ϕ	$-5/8$	$+5/8$	$-5/8$
			$+5/8$

hole pockets at the X points [182]. When the magnetic field is normal to the diamond-shaped Fermi surface, there are three extremal cross sections, the outer (α) and inner (β) cross sections of the diamond-shaped electron pocket, and the tubular-shaped hole pockets (γ). The α and β cross sections of the diamond-shaped Fermi surface take phase shifts of $5/8$ and $-5/8$, respectively. However, the frequencies of the α and β pockets are so large (about 10^4 T) that it is hard to be extracted from the experiments. In contrast, the γ nodal-line hole pockets have been identified as the origin of the high frequency (about 210 T) component [182]. This pocket encircles a nodal line, thus it has a π Berry phase. In addition, it has $\phi_{3D} = 0$ due to its quasi-2D nature. From Eq. (15), we find that the γ pocket has a phase shift of $\phi = -1/2 + \pi/2\pi + 0 = 0$, which is in agreement with the results obtained by Ali *et al.* [178]. In Ref. [9], we also analyzes the phase shifts for Cu₃PdN [77, 78].

When the symmetry protecting the nodal line is broken, there is a finite gap Δ that separates the conduction and valence bands. The Berry phase becomes

$$\phi_B = \pm\pi \left(1 - \frac{\Delta}{2E_F} \right). \quad (18)$$

The nodal-line semimetals may also be distinguished from their weak localization behaviors that cross between 2D weak anti-localization and 3D weak localization [197].

6 Strong field: 3D quantum Hall effect

The discovery of the quantum Hall effect in 2D opens the door to the field of topological phases of matter [198, 199]. In 3D electron gases, the extra dimension along the magnetic field direction prevents the quantization of the Hall conductance. Thus, the quantum Hall effect is normally observed in 2D systems [158, 198, 200–202]. In Ref. [7], we show a 3D quantum Hall effect in a topological semimetal. The topological semimetal can be considered as a 2D topological insulator for momenta (k_z here) between the Weyl nodes, resulting in the topologically protected surface states [in Fig. 4(c)] at the surfaces parallel to the Weyl node separation direction. The topologically protected states form the Fermi arcs [24, 26, 26, 29–34, 37–39, 42, 44, 203, 204] on the Fermi surface [red curves in

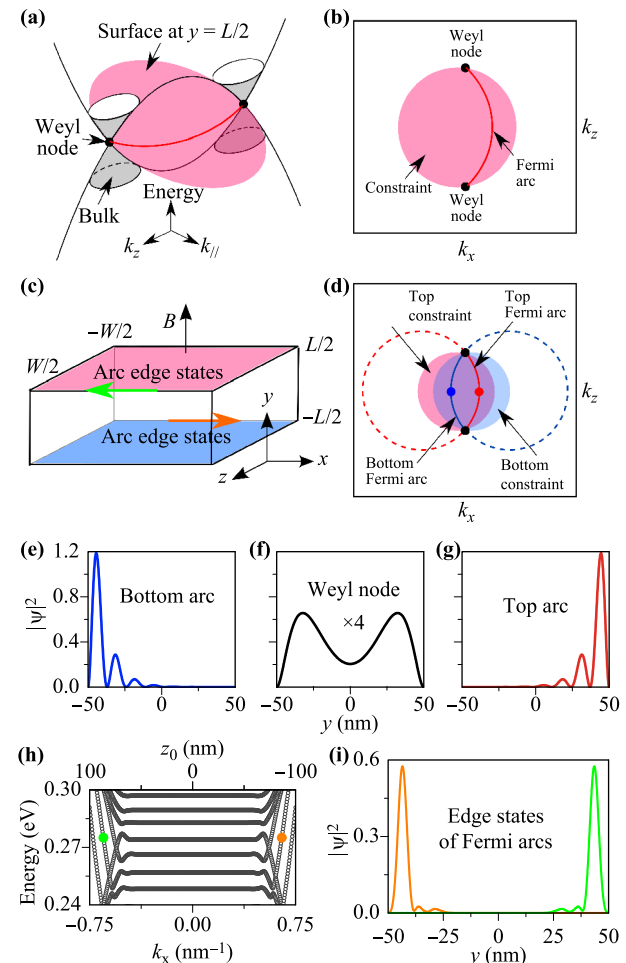


Fig. 4 (a) The energy dispersions for the Fermi arc (at $y = L/2$) and bulk states in a topological Weyl semimetal. $k_{/\!/}$ stands for (k_x, k_y) for the bulk and k_x for the arc, respectively. (b) The Fermi arc at $y = L/2$ and $E_F = E_w$ on the k_z - k_x plane. The shadow defines the “constraint” region where the Fermi arcs can exist. (c) A slab of topological semimetal of thickness L and width W . (d) The Fermi arcs at $E_F = E_w$ (solid) and constraints (shadow) at the $y = L/2$ (red) and $-L/2$ (blue) surfaces of the slab. [(e–g)] The wave function distributions at $k_z = 0$ along the y axis, at the blue (bottom arc, $k_x < 0$), black (Weyl nodes), and red (top arc, $k_x > 0$) dots in (d). (h) Landau levels of the Fermi arcs at $B = 5$ T vs. the guiding center z_0 . (i) The wave function distributions along the y axis for the edge states of the Fermi arcs marked by the green and orange dots in (h). $L = 100$ nm, $W = 200$ nm, and other parameters can be found in Fig. 5. Reproduced from Ref. [7].

Figs. 4 (a) and (b)]. The transport signature of the Fermi arcs is an intriguing topic [205–209].

6.1 Wormhole tunneling via Fermi arcs and Weyl nodes

The topological nature requires that only a region between the Weyl nodes can be occupied by the states of Fermi arcs [6] [Fig. 4(b)]. At one surface, a closed Fermi

loop, which is essential to the quantum Hall effect, cannot be formed by the Fermi arcs. However, in a topological semimetal slab, the Fermi arcs from opposite surfaces [Fig. 4(c)] can form the required closed Fermi loop [Fig. 4(d)]. Thus electrons can tunnel between the Fermi arcs at opposite surfaces via the Weyl nodes [Figs. 4(e)–(g)]. The Fermi loop formed by the Fermi arcs at opposite surfaces via the Weyl nodes can support a 3D quantum Hall effect. To be specific, the Weyl nodes act like “wormholes” that connect the top and bottom surfaces, and an electron can complete the cyclotron motion. Since the Weyl nodes are singularities in momentum, the wormhole tunneling can be infinite in real space, according to the uncertainty principle. The time scale of the “wormhole” tunneling is 0 as the Weyl node on the top surface and the Weyl node on the bottom surface are the same one and are described by the one coherence wavefunction. In experimental materials, the tunneling distance is limited by the mean free path, which can be comparable to or longer than 100 nm in high-mobility topological semimetals [43, 45, 46, 119, 160, 162, 167, 210, 211], even up to 1 μm [212], thus the thickness in the calculation is chosen to be 100 nm. The wormhole effect has been addressed in different situations in topological insulators [213]. The quantum Hall effect solely from the Fermi arcs requires the bulk carriers to be depleted by tuning the Fermi energy to the Weyl nodes [214]. Compared to the novel quantum oscillations [212, 215], the quantum Hall effect of the Fermi arcs contributes a quantized complement to the Fermi arc dominant electronic transports. The Weyl semimetals TaAs family [37–39, 42–46, 49–52, 210] and the Dirac semimetals Cd₃As₂ and Na₃Bi have extremely high mobilities [119, 160, 162, 167, 211] required by the quantum Hall effect. Low carrier densities [4, 35, 36] and gating [36] have also been achieved. The 3D quantum Hall effect of the Fermi arcs is expected in slabs of the TaAs family [37–39, 42–46, 210, 214], [110] or [1̄10] Cd₃As₂ [35, 216–219], and [100] or [010] Na₃Bi.

6.2 Quantized Hall conductance

We can calculate the Hall conductivity from the Kubo formula [7, 199, 220–224]. Figure 5(b) presents the sheet Hall conductivity σ_H^s for the topological semimetal slab. When the Fermi energy is far away from the Weyl nodes, the sheet Hall conductivity obeys the usual $1/B$ dependence. The closer the Fermi energy moves towards the Weyl nodes, the smaller the slope becomes, which indicates that the carrier density is decreasing. Moreover, when the Fermi energy moves towards the Weyl nodes, the quantized plateaus of σ_H^s begin to arise. Note that a 100-nm slab is still a 3D object.

6.3 3D distribution of the edge states

Figures 4(h) and (i) show that the edge states of the Fermi arcs have a unique 3D spatial distribution. Specifically,

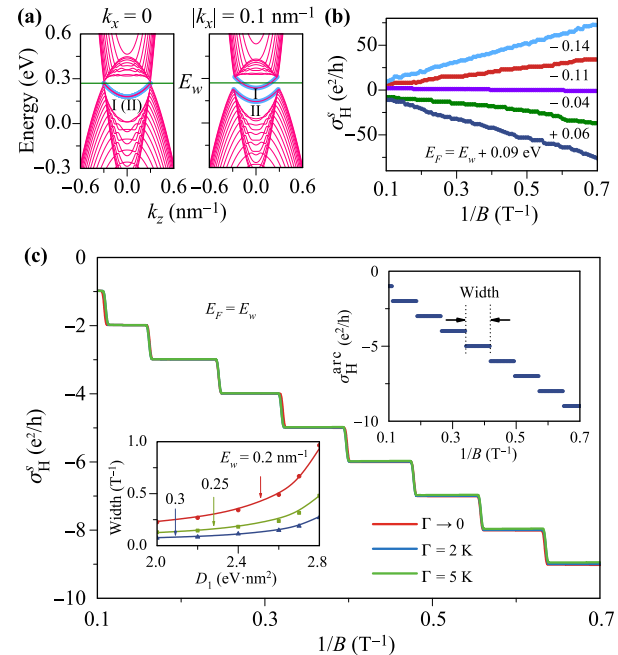


Fig. 5 (a) In a topological semimetal slab, the numerically calculated energy spectrum (pink) for the bulk states and Fermi arcs at $k_x = 0$ (left) and $k_x = \pm 0.1 \text{ nm}^{-1}$ (right). The blue curves are the Fermi arc bands plotted using H_{arc} and H'_{arc} . (b) The sheet Hall conductivity when the Fermi energy E_F crosses the bulk states for $\Gamma \rightarrow 0$. Γ is the disorder-induced level broadening. Recent experiments show that gating can tune carriers from n - to p -type in 100-nm-thick devices of topological semimetal [36]. (c) The sheet Hall conductivity σ_H^s at $E_F = E_w$, where the Fermi energy crosses only arc I. The right inset shows the analytic Hall conductance σ_H . In the presence of a residual detuning from the Weyl nodes, the bulk states also contribute to σ_H^s . Unlike that from the Fermi arcs, the contribution from the bulk states may change with the slab thickness. The left inset shows the width of the Hall plateaus in the clean limit as a function of D_1 for different k_w . The dots and lines are the numerical and analytic results, respectively. The parameters are $M = 5 \text{ eV}\cdot\text{nm}^2$, $A = 0.5 \text{ eV}\cdot\text{nm}$, and $D_2 = 3 \text{ eV}\cdot\text{nm}^2$, $D_1 = 2 \text{ eV}\cdot\text{nm}^2$, $k_w = 0.3 \text{ nm}^{-1}$, and $L = 100 \text{ nm}$. Reproduced from Ref. [7].

the top edge states propagate to the left (green arrow) and the bottom edge states to the right (orange arrow). This unique 3D distribution of the edge states of the Fermi arcs can be probed by scanning tunneling microscopy [225] or microwave impedance microscopy [226]. Different from topological insulators [201, 202], the Fermi-arc quantum Hall effect requires the collaboration of the two surfaces.

6.4 Topological Dirac semimetals

A single surface of the Dirac semimetal can form a complete Fermi loop needed by the quantum Hall effect due to the time-reversal symmetry. However, the single surface Fermi arc loop is not that robust and may be distorted [227]. Therefore, it may present different characteristics

compared to the two-surface Fermi arc loop. For the [112] and [110] Cd₃As₂ and [010] Na₃Bi [30] slabs, the parameters from Ref. [228] yield the 3D quantum Hall effect, which may exhibit a fourfold degeneracy.

7 Extremely strong field: Weyl fermion annihilation

The topological properties of the Weyl nodes can be revealed by studying the high-field transport properties of a Weyl semimetal. The lowest Landau bands of the Weyl cones remain at zero energy unless a strong magnetic field couples the Weyl fermions of opposite chirality. The coupled Weyl fermions lost their chiralities and acquire masses, two of the most characteristic features of the Weyl fermion. In this sense, the Weyl fermions are annihilated. In the Weyl semimetal TaP, we achieve such a magnetic coupling [11]. Their lowest Landau bands move above chemical potential, leading to a sharp sign reversal in the Hall resistivity at a specific magnetic field corresponding to the W₁ Weyl node separation. In the following, we use a model calculation to show the physics.

7.1 Calculation of Landau bands with magnetic fields in the x - z plane

In Section 2.1 of Ref. [1] and Eq. (1), we have given a minimal model for a Weyl semimetal

$$H = A(k_x \sigma_x + k_y \sigma_y) + \mathcal{M}_k \sigma_z, \quad (19)$$

where σ are the Pauli matrices, $\mathcal{M}_k = M_0 - M_1(k_x^2 + k_y^2 + k_z^2)$, $\mathbf{k} = (k_x, k_y, k_z)$ is the wave vector, and $A, M_{0/1}$ are model parameters. When $M_0 M_1 > 0$, the intersections of the two bands are at $(0, 0, \pm k_w)$ where $k_w \equiv \sqrt{M_0/M_1}$ (see Fig. 1 of [1]), leading to the topological semimetal phase.

In Section 2.6 of Ref. [1], we have given the Landau bands in a magnetic field along the z direction. Now we generalize the case to an arbitrary field applied normal to the y direction $\mathbf{B} = B(\sin \phi, 0, \cos \phi)$, where ϕ is the angle between the z and field directions. The Landau gauge can be chosen as $\mathbf{A} = (-B_z, 0, B_x)y$. Under the Pierls replacement

$$\mathbf{k} \rightarrow (k_x - y \cos \phi / \ell_B^2, -i\partial_y, k_z + y \sin \phi / \ell_B), \quad (20)$$

the Hamiltonian becomes $h(\mathbf{k}) \rightarrow$

$$\begin{pmatrix} j\mathcal{M}_k^B & A(k_x - y \cos \phi / \ell_B^2 - \partial_y) \\ A(k_x - y \cos \phi / \ell_B^2 + \partial_y) & -\mathcal{M}_k^B \end{pmatrix}, \quad (21)$$

where $\ell_B^2 \equiv \hbar/e|B|$ and $\mathcal{M}_k^B = M_1[k_c^2 - (k_x - y \cos \phi / \ell_B^2)^2 + \partial_y^2 - (k_z + y \sin \phi / \ell_B^2)^2]$. Define the guiding center

$$y_0 = \ell_B^2(k_x \cos \phi - k_z \sin \phi), \quad (22)$$

and the ladder operators [229]

$$\begin{aligned} a &= -\frac{1}{\sqrt{2}} \left(\frac{y - y_0}{\ell_B} + \ell_B \partial_y \right), \\ a^\dagger &= -\frac{1}{\sqrt{2}} \left(\frac{y - y_0}{\ell_B} - \ell_B \partial_y \right), \end{aligned} \quad (23)$$

the Hamiltonian becomes

$$h_a = \begin{pmatrix} \mathcal{M}_a & \mathcal{A}_a^- \\ \mathcal{A}_a^+ & -\mathcal{M}_a \end{pmatrix}, \quad (24)$$

where

$$\begin{aligned} \mathcal{M}_a &= M_1 \left[k_c^2 - k_{//}^2 - \frac{2}{\ell_B^2} \left(a^\dagger a + \frac{1}{2} \right) \right], \\ \mathcal{A}_a^\pm &= A \left(k_{//} \sin \phi + \frac{\cos \phi \mp 1}{\sqrt{2}\ell_B} a + \frac{\cos \phi \pm 1}{\sqrt{2}\ell_B} a^\dagger \right). \end{aligned} \quad (25)$$

We have defined $k_{//} = k_x \sin \phi + k_z \cos \phi$, which is the summation of the projections of k_x and k_z along the direction of the magnetic field and can serve as a good quantum number.

7.2 Landau bands in the z -direction magnetic field

At $\phi = 0$, i.e., the magnetic field is applied along the z direction, the Hamiltonian reduces to

$$h_a = \begin{pmatrix} \mathcal{M}_a & \eta a \\ \eta a^\dagger & -\mathcal{M}_a \end{pmatrix}, \quad (26)$$

where $\mathcal{M}_a = M_0 - M_1 k_z^2 - \omega(a^\dagger a + 1/2)$, $\eta = \sqrt{2}A/\ell_B$, $\omega = 2M_1/\ell_B^2$. With the trial wave functions $(c_1|\nu-1\rangle, c_2|\nu\rangle)^T$ for $\nu = 1, 2, \dots$ (later denoted as $\nu \geq 1$) and $(0, |0\rangle)^T$ for $\nu = 0$, where ν indexes the Hermite polynomials, the eigen energies E can be found from the secular equation

$$\det \begin{pmatrix} \mathcal{M}_\nu + \omega/2 - E & \eta\sqrt{\nu} \\ \eta\sqrt{\nu} & -\mathcal{M}_\nu + \omega/2 - E \end{pmatrix} = 0 \quad (27)$$

for $\nu \geq 1$, and $-\mathcal{M}_\nu + \omega/2 - E = 0$ for $\nu = 0$, where $\mathcal{M}_\nu = M_0 - M_1 k_z^2 - \omega\nu$. The eigen energies are found as

$$\begin{aligned} E_{k_z}^{\nu\pm} &= \omega/2 \pm \sqrt{\mathcal{M}_\nu^2 + \nu\eta^2}, \quad \nu \geq 1 \\ E_{k_z}^0 &= \omega/2 - M_0 + M_1 k_z^2, \quad \nu = 0. \end{aligned} \quad (28)$$

They represent a set of Landau energy bands (ν as band index) dispersing with k_z . The eigen states for $\nu \geq 1$ are

$$\begin{aligned} |\nu \geq 1, k_x, k_z, +\rangle &= \begin{pmatrix} \cos \frac{\theta_{k_z}^\nu}{2} |\nu-1\rangle \\ \sin \frac{\theta_{k_z}^\nu}{2} |\nu\rangle \end{pmatrix} |k_x, k_z\rangle, \\ |\nu \geq 1, k_x, k_z, -\rangle &= \begin{pmatrix} \sin \frac{\theta_{k_z}^\nu}{2} |\nu-1\rangle \\ -\cos \frac{\theta_{k_z}^\nu}{2} |\nu\rangle \end{pmatrix} |k_x, k_z\rangle, \end{aligned} \quad (29)$$

and for $\nu = 0$ is

$$|\nu = 0, k_x, k_z\rangle = \begin{bmatrix} 0 \\ |0\rangle \end{bmatrix} |k_x, k_z\rangle,$$

where $\cos\theta = \mathcal{M}_\nu/\sqrt{\mathcal{M}_\nu^2 + \nu\eta^2}$, and the wave functions $\psi_{\nu,k_z,k_x}(\mathbf{r}) = \langle \mathbf{r} | \nu, k_x, k_z \rangle$ are found as

$$\psi_{\nu,k_z,k_x}(\mathbf{r}) = \frac{C_\nu}{\sqrt{L_x L_z \ell_B}} e^{ik_z z} e^{ik_x x} e^{-\frac{(y-y_0)^2}{2\ell_B^2}} \mathcal{H}_\nu \left(\frac{y-y_0}{\ell_B} \right), \quad (30)$$

where $C_\nu \equiv 1/\sqrt{\nu! 2^\nu \sqrt{\pi}}$, $L_x L_z$ is the area of the sample, the guiding center $y_0 = k_x \ell_B^2$, \mathcal{H}_ν are the Hermite

polynomials. As the dispersions are not explicit functions of k_x , the number of different k_x represents the Landau degeneracy $N_L = 1/(2\pi\ell_B^2) = eB/h$ in a unit area in the $x-y$ plane.

7.3 Landau bands in the x -direction magnetic field

If $\phi \neq 0$, the Hamiltonian can be solved numerically. We can write Eq. (24) as

$$\begin{aligned} h_a &= h_a^{(0)} + h'_a, \\ h_a^{(0)} &= \begin{pmatrix} \mathcal{M}_a & Ak_{//} \sin \phi \\ Ak_{//} \sin \phi & -\mathcal{M}_a \end{pmatrix}, \\ h'_a &= \begin{pmatrix} 0 & \eta \left(\frac{\cos \phi + 1}{2} a + \frac{\cos \phi - 1}{2} a^\dagger \right) \\ \eta \left(\frac{\cos \phi - 1}{2} a + \frac{\cos \phi + 1}{2} a^\dagger \right) & 0 \end{pmatrix}, \end{aligned} \quad (31)$$

where $k_{//} = k_x \sin \phi + k_z \cos \phi$, $\mathcal{M}_a = M_1[k_c^2 - k_{//}^2 - \frac{2}{\ell_B^2}(a^\dagger a + \frac{1}{2})]$ and $\eta = \sqrt{2}A/\ell_B$. $H_a^{(0)}$ can be readily diagonalized to give the band spectrum

$$E_k^{\nu\pm} = \pm \sqrt{\mathcal{M}_\nu^2 + (Ak_{//} \sin \phi)^2}, \quad (32)$$

where $\mathcal{M}_\nu \equiv M_1[k_c^2 - k_{//}^2 - \frac{2}{\ell_B^2}(\nu + \frac{1}{2})]$. The wave functions for the conduction and valence bands are

$$\begin{aligned} |\nu, +, k_{//}\rangle^{(0)} &= \begin{pmatrix} \cos \frac{\Theta_{k_{//}}^\nu}{2} \\ \sin \frac{\Theta_{k_{//}}^\nu}{2} \end{pmatrix}, \\ |\nu, -, k_{//}\rangle^{(0)} &= \begin{pmatrix} \sin \frac{\Theta_{k_{//}}^\nu}{2} \\ -\cos \frac{\Theta_{k_{//}}^\nu}{2} \end{pmatrix}, \end{aligned} \quad (33)$$

with $\cos \Theta_{k_{//}}^\nu \equiv \mathcal{M}_\nu/E_{k_{//}}^{\nu+}$, $\sin \Theta_{k_{//}}^\nu \equiv Ak_{//} \sin \theta/E_{k_x}^{\nu+}$. Denote

$$\begin{aligned} A_{\mu,\nu} &= A \left(\frac{\cos \phi + 1}{\sqrt{2}\ell_B} \sqrt{\nu} \delta_{\mu,\nu-1} + \frac{\cos \phi - 1}{\sqrt{2}\ell_B} \sqrt{\nu + 1} \delta_{\mu,\nu+1} \right), \\ A_{\mu,\nu}^\dagger &= A \left(\frac{\cos \phi - 1}{\sqrt{2}\ell_B} \sqrt{\nu} \delta_{\mu,\nu-1} + \frac{\cos \phi + 1}{\sqrt{2}\ell_B} \sqrt{\nu + 1} \delta_{\mu,\nu+1} \right), \end{aligned} \quad (34)$$

we can calculate the off-diagonal matrix elements in the basis of $|\nu, \pm, k_{//}\rangle^{(0)}$ as

$$\begin{aligned} &\langle \mu, +, k_{//} | H'_a | \nu, +, k_{//} \rangle \\ &= A_{\mu,\nu} \cos \frac{\Theta_{k_{//}}^\mu}{2} \sin \frac{\Theta_{k_{//}}^\nu}{2} + A_{\mu,\nu}^\dagger \sin \frac{\Theta_{k_{//}}^\mu}{2} \cos \frac{\Theta_{k_{//}}^\nu}{2}, \\ &\langle \mu, -, k_{//} | H'_a | \nu, -, k_{//} \rangle \\ &= -A_{\mu,\nu} \sin \frac{\Theta_{k_{//}}^\mu}{2} \cos \frac{\Theta_{k_{//}}^\nu}{2} - A_{\mu,\nu}^\dagger \cos \frac{\Theta_{k_{//}}^\mu}{2} \sin \frac{\Theta_{k_{//}}^\nu}{2}, \end{aligned}$$

$$\begin{aligned} &\langle \mu, +, k_{//} | H'_a | \nu, -, k_{//} \rangle \\ &= -A_{\mu,\nu} \cos \frac{\Theta_{k_{//}}^\mu}{2} \cos \frac{\Theta_{k_{//}}^\nu}{2} + A_{\mu,\nu}^\dagger \sin \frac{\Theta_{k_{//}}^\mu}{2} \sin \frac{\Theta_{k_{//}}^\nu}{2}, \\ &\langle \mu, -, k_{//} | H'_a | \nu, +, k_{//} \rangle \\ &= A_{\mu,\nu} \sin \frac{\Theta_{k_{//}}^\mu}{2} \sin \frac{\Theta_{k_{//}}^\nu}{2} - A_{\mu,\nu}^\dagger \cos \frac{\Theta_{k_{//}}^\mu}{2} \cos \frac{\Theta_{k_{//}}^\nu}{2}. \end{aligned} \quad (35)$$

Then the energy spectrum along arbitrary directions in the $x-z$ plane can be solved numerically.

Figure 6 shows the Landau bands of the Weyl semimetal. When the magnetic field is along the z direction ($\theta = 0$), the lowest Landau band (red) crosses the Fermi energy (dashed line). As the magnetic field is ro-

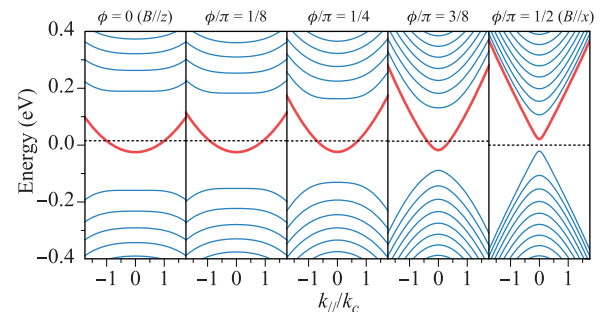


Fig. 6 For the two-node model for Weyl semimetals [Eq. (19)], the energy spectrum of the Landau bands in a magnetic field \mathbf{B} applied normal to the y direction, as functions of the wave vector $k_{//} \equiv k_x \sin \phi + k_z \cos \phi$ that is parallel to \mathbf{B} . ϕ is defined by $\tan \phi = B_x/B_z$. The red curve is the 0th Landau bands. The dashed line is the Fermi energy. The parameters $k_w = 0.2 \text{ nm}^{-1}$, $M_1 = 1 \text{ eV}\cdot\text{nm}^2$, $A = 1 \text{ eV}\cdot\text{nm}$, and $B = 10 \text{ T}$. The number of the Landau bands used in the numerical diagonalization is 401.

tated from the z direction to the x direction ($\theta = \pi/2$), the lowest Landau band is shifted and evolving. When the magnetic field is along the x direction, the spectrum of the Landau bands is particle-hole symmetric and there is a gap due to the coupling between the Weyl fermions at the opposite Weyl nodes. This gap is why there is a sharp sign reversal in the Hall resistivity in the strong-field quantum limit of the Weyl semimetal TaP [11]. Because of the gap, the Weyl fermions acquire masses and lose their chiralities. Since having chirality and no mass are two features of the Weyl fermion, the Hall signal therefore indicates that the Weyl fermions are annihilated.

8 Extremely strong field: Forbidden backscattering and resistance dip in the quantum limit

The discovery of 3D topological insulators [58, 230, 231], whose characteristics is of topologically protected 2D surface states, shines light on the exploring of exotic topological phases [232–237]. Therefore, distinguishing the bulk-state transport to identify topological insulators is an intriguing topic.

In strong magnetic fields, 1D Landau bands are formed from the quantization of the bulk states of a 3D topological insulator. In 2D, lowest Landau levels cross each other, which servers as a signature for the quantum spin Hall phase [238, 239]. In 2D, other approaches can be deployed to probe the quantum spin Hall phase, for example, interference effects [240]. However, in 3D, it is seldom addressed that whether the lowest Landau band could be used to identify a topological insulator. In Ref. [12], we study the resistance of a 3D topological insulator in the strong-field quantum limit, namely, only the lowest Landau band is occupied [Fig. 7(b)]. We find that the backscattering can be totally suppressed in the quantum limit at a critical magnetic field, which can be used to identify the topological insulator phases. Besides, this forbidden backscattering is absent in topological semimetals [5, 6, 147]. This theory is consistent with the recent experiment [Figs. 7(c) and (d)]. Moreover, this mechanism will be practical for those materials with small gap, for example, the ZrTe₅ [241, 242] families and the Ag₂Te [243].

8.1 Forbidden backscattering in the quantum limit

In a strong magnetic field B along the z direction, the energy spectrum quantizes into a series of 1D Landau bands [Figs. 7(a) and (b)]. The energies of the lowest two Landau bands, denoted as $0+$ and $0-$, are $E_{0\pm} = C_0 + C_z k_z^2 + C_\perp / \ell_B^2 \pm \sqrt{m^2 + V_n^2 k_z^2}$, where the magnetic length $\ell_B \equiv \sqrt{\hbar/eB}$, the electron charge $-e$, and the mass term

$$m = M_0 + M_z k_z^2 + M_\perp / \ell_B^2. \quad (36)$$

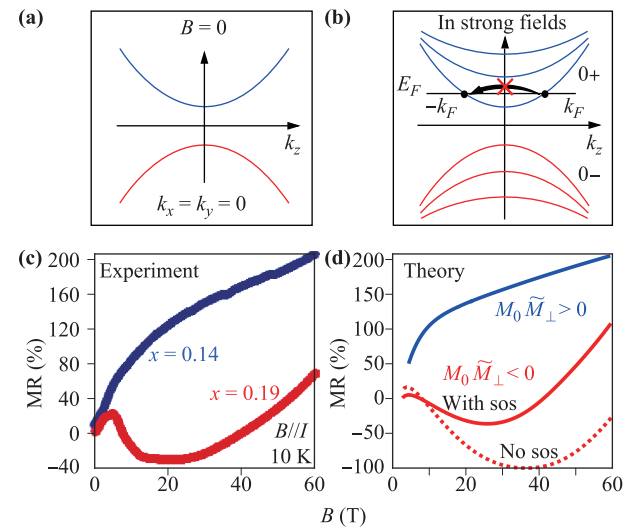


Fig. 7 In the quantum limit of a 3D topological insulator, the backscattering between the only two states at the Fermi energy can be forbidden at a critical magnetic field, leading to a resistance dip. (a) The zero-field energy spectrum vs. k_z of a 3D topological insulator at $k_x = k_y = 0$. (b) In a strong magnetic field, the lowest Landau energy bands of the 3D topological insulator vs. k_z . The Fermi energy E_F crosses only the $0+$ Landau band. k_F and $-k_F$ stand for the only two states at the Fermi energy. (c) The magnetoresistance of $Pb_{1-x}Sn_xSe$ reproduced from Ref. [125]. (d) The calculated magnetoresistance. The abbreviation “sos” means spin-orbit scattering. The parameters are $M_0 = -0.01$ eV, $M_z = 0$, $M_\perp = 18$ eV·Å², $\alpha_1 = 100$ eV·T, and $\alpha_2 = 0.0025$ eV·T⁻². Reproduced from Ref. [12].

We can determine the gap between the two lowest Landau bands by m with $k_z = 0$.

Next, we will concentrate on an electron-doped quantum limit, namely, the Fermi energy intersects only with the $0+$ Landau band, of which the eigenstate is

$$|0, +, k_x, k_z\rangle = \begin{pmatrix} 0 \\ -i \sin(\theta/2) \\ 0 \\ \cos(\theta/2) \end{pmatrix} |0, k_x, k_z\rangle, \quad (37)$$

where we have defined

$$\cos \theta \equiv \frac{-m}{\sqrt{m^2 + (V_n k_z)^2}}, \quad (38)$$

and $|0, k_x, k_z\rangle$ is the state of a usual zeroth Landau level multiplying a plane wave function along the z direction [5].

In solids, the electronic transport is relatively influenced by the backscattering, which plays a dictating role in the presence of the 1D Landau band, since there are only two states at the Fermi energy, as denoted by k_F and $-k_F$ in Fig. 7. The backscattering between these two states is characterized by the scattering matrix element between them. From the spinor eigenstate in Eq. (37), we find that the modular square of the scattering matrix element

between the k_F and $-k_F$ states is in proportion to the form factor

$$I_S = \cos^2 \theta|_{k_z=k_F}. \quad (39)$$

I_S vanishes when $m = 0$, that is, the backscattering between state k_F and state $-k_F$ is forbidden. According to Eq. (36), m vanishes at a critical magnetic field B_c evaluated by $M_0 + M_z k_F^2 + M_\perp eB_c/\hbar = 0$, where k_z is equal to the Fermi wave vector k_F at the Fermi energy. For a topological insulator, $M_0 M_z < 0$ and $M_0 M_\perp < 0$, thus B_c holds finite solutions, at which the backscattering is totally suppressed. A rich phase diagram can be found in Fig. 8. This forbidden backscattering will result in a dip in the resistance as a function of the magnetic field, which can be probed in experiments and can serve as a signature for topological insulator phases. This forbidden backscattering is an eigenstate property and thus is new and different from the mechanism of Landau level crossing [238, 239], which is a spectrum property.

8.2 Conductivity in the quantum limit

Along the direction of the magnetic field, there is no Hall effect, thus the resistivity is the inverse of the conductivity, namely, $\rho_{zz} = 1/\sigma_{zz}$. In the quantum limit, only band 0+ contributes to the conductivity. Following the methods in

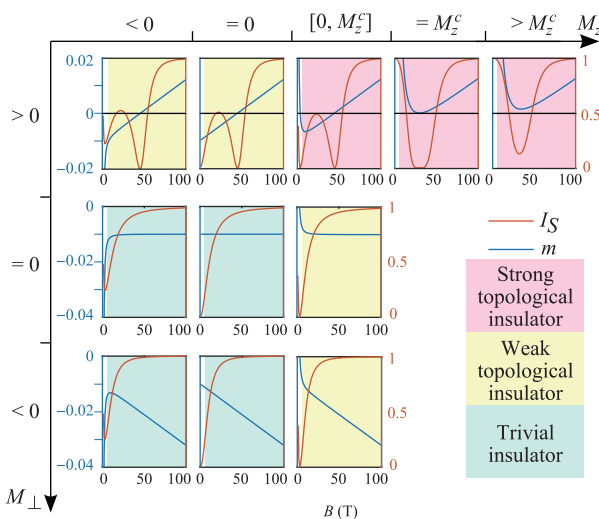


Fig. 8 The mass term m and form factor I_S as functions of the magnetic field B for $M_0 < 0$ and different M_\perp and M_z . Red, yellow, and green backgrounds indicate the quantum limit for a carrier density of $6 \times 10^{16}/\text{cm}^3$. Without loss of generality, we have assumed $M_0 < 0$, so $M_\perp > 0$ and $M_z > 0$ means strong a topological insulator, $M_\perp \leq 0$ and $M_z \leq 0$ means a trivial insulator, $M_\perp \leq 0$ and $M_z > 0$ means a weak topological insulator (001) and $M_\perp > 0$ and $M_z \leq 0$ means a weak topological insulator (110). The parameters are $M_0 = -0.01 \text{ eV}$, $M_z = -27, 0, 27, 820, 1200 \text{ eV}\cdot\text{\AA}^2$ from left to right, $M_\perp = -13.5, 0, 13.5 \text{ eV}\cdot\text{\AA}^2$ from bottom to top. Reproduced from Ref. [12].

Refs. [5, 6, 244], the resistivity can be expressed as

$$\rho_{zz} = I_S/\sigma_0, \quad (40)$$

where σ_0 is the conductivity independent of the spinor inner product part and I_S is the form factor. For different types of scattering potential, σ_0 takes different forms. However, the form factor I_S in Eq. (40) indicates that, for a topological insulator, the resistance always has a dip, regardless of σ_0 . Figure 4 in Ref. [12] reveals the resistivity when the Gaussian and screened Coulomb potentials are present. They both show clear dips in the resistivity for some weak topological phases ($M_z \leq 0$ and $\tilde{M}_\perp > 0$ in row 1, columns 1 and 2) and strong topological insulator phases ($M_z \in [0, M_z^c]$ and $\tilde{M}_\perp > 0$ in row 1, column 3). Furthermore, the positions of the minima on the B axis do not change for various potentials. The spin-orbit scattering can improve the above picture and result in a better fitting to the experiment. Specifically, in Fig. 7(d), the spin-orbit coupling is included in the screened Coulomb scattering potential. By choosing proper fitting parameters, we obtain a -40% change at the dip of the resistance, which is in agreement with the experiment, as shown in Figs. 7(c) and (d).

9 Remarks and perspective

The theories of the quantum oscillations need to be improved to match the semiclassical argument and full quantum mechanics calculations. Recently, a quantum theory of intrinsic magnetoresistance for three-dimensional Dirac fermions in a uniform magnetic field is proposed, which shows that the relative magneto-resistance is inversely quartic of the Fermi wave vector and only determined by carrier density, and a formula for the phase shift in SdH oscillation is present as a function of the mobility and the magnetic field [245]. Furthermore, new discoveries on quantization rules in oscillations have been found for graphene, 2D materials, topological metals, topological crystalline insulator, and Dirac and Weyl semimetals [246, 247]. Topological contributions have also been found in Bloch oscillations [248]. Generalizations of these classical notions to nodal-line systems will be topics of fundamental interests in the future. Whether the rules for phase shift can be generalized to extremal orbits shared by electron and hole pockets in type-II Weyl semimetals [246, 249] will be an outstanding problem. Quantum oscillations in type-II Dirac semimetals PdTe₂ [250] and nodal-line systems [251, 252] have also been addressed.

Lately, the quantized Hall resistance plateaus have been experimentally observed in the topological semimetal Cd₃As₂ [217, 218, 253], with thickness ranging from 10 to 80 nm. They cannot be regarded as 2D. Nevertheless, several questions still hold. First, Cd₃As₂ is a Dirac semimetal, composed of two time-reversed Weyl semimetals. At a single surface, there is a complete 2D electron

gas, formed by two time-reversed half 2D electron gases of the Fermi-arc surface states. There may be also the trivial quantum Hall effect on a single surface. Second, the 3D bulk states quantize into 2D subbands for those thicknesses. If the 3D bulk states cannot be depleted entirely, they also have the trivial quantum Hall effect. The two issues may explain the 2-fold and 4-fold degenerate Hall resistance plateaus observed in the experiments. To deplete the 3D bulk states, the Fermi energy has to be placed exactly at the Weyl nodes. How to distinguish these trivial mechanisms from the 3D quantum Hall effect will be an interesting direction. Previously, when studying the geometric phase, the parameter space is usually either in real space or momentum space [131]. The Weyl orbit formed by the Fermi arcs and Weyl nodes is a new physics, because part of the geometric phase is accumulated in real space and part in momentum space, quite different from the parameter spaces studied before. In particular, the geometric phase has a thickness dependence when accumulated along the path as electrons tunnel between the top and bottom surfaces [215, 254]. Recently, a new experiment uses this thickness-dependent phase shift to demonstrate the contribution of the Weyl orbit in the observed quantized Hall resistance [219]. The 3D quantum Hall effect can also be supported by the CDW mechanism [255], which has been observed recently in ZrTe₅ [256]. More works will be inspired to verify the mechanism and realize the 3D quantum Hall effect in the future [257].

In the quantum limit, our theory have shown that up to two resistance dips may appear if the system is a 3D strong topological insulator [12]. Surprisingly, recent experiments report up to five oscillations in the quantum limit [258, 259]. The oscillation as a function of the magnetic field follows a logarithmic scale invariance law, much like those in the Efimov bound states of cold atoms. The Efimov bound state is a three-body bound state arising from the two-body interactions between atoms. Efimov-like bound states have been used to understand the unexpected oscillations [260, 261]. A direct fitting of the resistance in the experiment have also been demonstrated [258, 259, 261]. Nevertheless, other mechanisms that may lead to the scale invariance oscillations will be topics of broad interest.

In solids, the space group can protect energy nodes with other degeneracies, such as three-, six- and eight-fold one, which may lead to massless fermions that have no counterpart particles in high-energy physics [262–265]. Triply-degenerate nodal-point semimetals have been proposed with symmorphic space group symmetry of WC type crystal structure, including TaN, ZrTe and MoP, and observed by angle-resolved photoemission spectroscopy [266, 267]. The unconventional three component fermions in them are formed by crossing of nondegenerate and double degenerate bands, protected by both rotational and mirror symmetries. As an intermediate fermion between Dirac and Weyl fermion, the host semimetal is expected

to have different magnetoresistance [268–270]. More topics will also be of broad interest, including the quantum transport in magnetic Weyl semimetals [56, 271–279], the kagome ferromagnet Fe₃Sn₂ [280], double-Weyl semimetals [20, 281], type-II Weyl semimetals [51, 282–291], hopf-link nodal-line semimetals [292–295], Aharonov-Bohm effect [296], quasiparticle interference on the surfaces of Weyl semimetals [297–300] and Fano effect [301], exploring axial-gravitational anomaly through thermoelectrical transport [302].

Acknowledgements This work was supported by Guangdong Innovative and Entrepreneurial Research Team Program (Grant No. 2016ZT06D348), the National Key R & D Program (Grant No. 2016YFA0301700), the National Natural Science Foundation of China (Grant No. 11574127), and the Science, Technology, and Innovation Commission of Shenzhen Municipality (Grant Nos. ZDSYS20170303165926217 and JCYJ20170412152620376).

References

1. H.-Z. Lu and S.-Q. Shen, Quantum transport in topological semimetals under magnetic fields, *Front. Phys.* 12, 127201 (2017)
2. H. Z. Lu and S. Q. Shen, Weak antilocalization and localization in disordered and interacting Weyl semimetals, *Phys. Rev. B* 92, 035203 (2015)
3. X. Dai, H.-Z. Lu, S.-Q. Shen, and H. Yao, Detecting monopole charge in Weyl semimetals via quantum interference transport, *Phys. Rev. B* 93, 161110(R) (2016)
4. H. Li, H. T. He, H. Z. Lu, H. C. Zhang, H. C. Liu, R. Ma, Z. Y. Fan, S. Q. Shen, and J. N. Wang, Negative magnetoresistance in Dirac semimetal Cd₃As₂, *Nat. Commun.* 7, 10301 (2016)
5. H. Z. Lu, S. B. Zhang, and S. Q. Shen, High-field magnetocconductivity of topological semimetals with short-range potential, *Phys. Rev. B* 92, 045203 (2015)
6. S.-B. Zhang, H.-Z. Lu, and S.-Q. Shen, Linear magnetocconductivity in an intrinsic topological Weyl semimetal, *New J. Phys.* 18, 053039 (2016)
7. C. M. Wang, H.-P. Sun, H.-Z. Lu, and X. C. Xie, 3D quantum Hall effect of Fermi arcs in topological semimetals, *Phys. Rev. Lett.* 119, 136806 (2017)
8. C. M. Wang, H.-Z. Lu, and S.-Q. Shen, Anomalous phase shift of quantum oscillations in 3D topological semimetals, *Phys. Rev. Lett.* 117, 077201 (2016)
9. C. Li, C. M. Wang, B. Wan, X. Wan, H.-Z. Lu, and X. C. Xie, Rules for phase shifts of quantum oscillations in topological nodal-line semimetals, *Phys. Rev. Lett.* 120, 146602 (2018)
10. X. Dai, Z. Z. Du, and H.-Z. Lu, Negative magnetoresistance without chiral anomaly in topological insulators, *Phys. Rev. Lett.* 119, 166601 (2017)
11. C.-L. Zhang, *et al.*, Magnetic-tunnelling-induced Weyl node annihilation in TaP, *Nat. Phys.* 13, 979 (2017)

12. Y. Chen, H.-Z. Lu, and X. C. Xie, Forbidden backscattering and resistance dip in the quantum limit as a signature for topological insulators, *Phys. Rev. Lett.* 121, 036602 (2018)
13. H. Weng, X. Dai, and Z. Fang, Topological semimetals predicted from first-principles calculations, *J. Phys.: Condens. Matter* 28, 303001 (2016)
14. B. Yan and C. Felser, Topological materials: Weyl semimetals, *Ann. Rev. Condens. Matter Phys.* 8, 337 (2017)
15. N. P. Armitage, E. J. Mele, and A. Vishwanath, Weyl and Dirac semimetals in three-dimensional solids, *Rev. Mod. Phys.* 90, 015001 (2018)
16. H. Wang and J. Wang, Electron transport in Dirac and Weyl semimetals, *Chin. Phys. B* 27, 107402 (2018)
17. X. Wan, A. M. Turner, A. Vishwanath, and S. Y. Savrasov, Topological semimetal and Fermi-arc surface states in the electronic structure of pyrochlore iridates, *Phys. Rev. B* 83, 205101 (2011)
18. K. Y. Yang, Y. M. Lu, and Y. Ran, Quantum Hall effects in a Weyl semimetal: Possible application in pyrochlore iridates, *Phys. Rev. B* 84, 075129 (2011)
19. A. A. Burkov and L. Balents, Weyl semimetal in a topological insulator multilayer, *Phys. Rev. Lett.* 107, 127205 (2011)
20. G. Xu, H. M. Weng, Z. J. Wang, X. Dai, and Z. Fang, Chern semimetal and the quantized anomalous Hall effect in $HgCr_2Se_4$, *Phys. Rev. Lett.* 107, 186806 (2011)
21. P. Delplace, J. Li, and D. Carpentier, Topological Weyl semi-metal from a lattice model, *EPL* 97, 67004 (2012)
22. J.-H. Jiang, Tunable topological Weyl semimetal from simple-cubic lattices with staggered fluxes, *Phys. Rev. A* 85, 033640 (2012)
23. S. M. Young, S. Zaheer, J. C. Y. Teo, C. L. Kane, E. J. Mele, and A. M. Rappe, Dirac semimetal in three dimensions, *Phys. Rev. Lett.* 108, 140405 (2012)
24. Z. Wang, Y. Sun, X. Q. Chen, C. Franchini, G. Xu, H. Weng, X. Dai, and Z. Fang, Dirac semimetal and topological phase transitions in A_3Bi ($A = Na, K, Rb$), *Phys. Rev. B* 85, 195320 (2012)
25. B. Singh, A. Sharma, H. Lin, M. Z. Hasan, R. Prasad, and A. Bansil, Topological electronic structure and Weyl semimetal in the $TlBiSe_2$ class of semiconductors, *Phys. Rev. B* 86, 115208 (2012)
26. Z. Wang, H. Weng, Q. Wu, X. Dai, and Z. Fang, Three-dimensional Dirac semimetal and quantum transport in Cd_3As_2 , *Phys. Rev. B* 88, 125427 (2013)
27. J. Liu and D. Vanderbilt, Weyl semimetals from non-centrosymmetric topological insulators, *Phys. Rev. B* 90, 155316 (2014)
28. D. Bulmash, C.-X. Liu, and X.-L. Qi, Prediction of a Weyl semimetal in $HgCdMnTe$, *Phys. Rev. B* 89, 081106 (2014)
29. Z. K. Liu, *et al.*, Discovery of a three-dimensional topological Dirac semimetal, *Science* 343, 864 (2014)
30. S. Y. Xu, *et al.*, Observation of Fermi arc surface states in a topological metal, *Science* 347, 294 (2015)
31. Z. K. Liu, *et al.*, A stable three-dimensional topological Dirac semimetal Cd_3As_2 , *Nat. Mater.* 13, 677 (2014)
32. M. Neupane, *et al.*, Observation of a three-dimensional topological Dirac semimetal phase in high-mobility Cd_3As_2 , *Nat. Commun.* 5, 3786 (2014)
33. S. Borisenko, Q. Gibson, D. Evtushinsky, V. Zabolotnyy, B. Büchner, and R. J. Cava, Experimental realization of a three-dimensional Dirac semimetal, *Phys. Rev. Lett.* 113, 027603 (2014)
34. H. Yi, *et al.*, Evidence of topological surface state in three-dimensional Dirac semimetal Cd_3As_2 , *Sci. Rep.* 4, 6106 (2014)
35. C. Zhang, *et al.*, Room-temperature chiral charge pumping in Dirac semimetals, *Nat. Commun.* 8, 13741 (2017)
36. C. Z. Li, L. X. Wang, H. W. Liu, J. Wang, Z. M. Liao, and D. P. Yu, Giant negative magnetoresistance induced by the chiral anomaly in individual Cd_3As_2 nanowires, *Nat. Commun.* 6, 10137 (2015)
37. S. M. Huang, *et al.*, A Weyl fermion semimetal with surface Fermi arcs in the transition metal monopnictide TaAs class, *Nat. Commun.* 6, 7373 (2015)
38. H. M. Weng, C. Fang, Z. Fang, B. A. Bernevig, and X. Dai, Weyl semimetal phase in noncentrosymmetric transition-metal monophosphides, *Phys. Rev. X* 5, 011029 (2015)
39. B. Q. Lv, *et al.*, Experimental discovery of Weyl semimetal TaAs, *Phys. Rev. X* 5, 031013 (2015)
40. B. Q. Lv, *et al.*, Observation of Weyl nodes in TaAs, *Nat. Phys.* 11, 724 (2015)
41. B. Q. Lv, *et al.*, Observation of Fermi-arc spin texture in TaAs, *Phys. Rev. Lett.* 115, 217601 (2015)
42. S. Y. Xu, *et al.*, Discovery of a Weyl fermion semimetal and topological Fermi arcs, *Science* 349, 613 (2015)
43. L. X. Yang, *et al.*, Weyl semimetal phase in the non-centrosymmetric compound TaAs, *Nat. Phys.* 11, 728 (2015)
44. Z. K. Liu, *et al.*, Evolution of the Fermi surface of Weyl semimetals in the transition metal pnictide family, *Nat. Mater.* 15, 27 (2015)
45. C. L. Zhang, *et al.*, Signatures of the Adler–Bell–Jackiw chiral anomaly in a Weyl Fermion semimetal, *Nat. Commun.* 7, 10735 (2016)
46. X. C. Huang, *et al.*, Observation of the chiral-anomaly-induced negative magnetoresistance in 3D Weyl semimetal TaAs, *Phys. Rev. X* 5, 031023 (2015)
47. S.-Y. Xu, *et al.*, Discovery of a Weyl fermion state with Fermi arcs in niobium arsenide, *Nat. Phys.* 11, 748 (2015)
48. N. Xu, *et al.*, Observation of Weyl nodes and Fermi arcs in tantalum phosphide, *Nat. Commun.* 7, 11006 (2016)
49. S.-Y. Xu, *et al.*, Spin polarization and texture of the Fermi arcs in the Weyl fermion semimetal TaAs, *Phys. Rev. Lett.* 116, 096801 (2016)

50. I. Belopolski, *et al.*, Criteria for directly detecting topological Fermi arcs in Weyl semimetals, *Phys. Rev. Lett.* 116, 066802 (2016)
51. I. Belopolski, *et al.*, Fermi arc electronic structure and Chern numbers in the type-II Weyl semimetal candidate $\text{Mo}_x \text{W}_{1-x} \text{Te}_2$, *Phys. Rev. B* 94, 085127 (2016)
52. S.-Y. Xu, *et al.*, Experimental discovery of a topological weyl semimetal state in tap, *Sci. Adv.* 1, 10 (2015)
53. I. Belopolski, *et al.*, Signatures of a time-reversal symmetric Weyl semimetal with only four Weyl points, *Nat. Commun.* 8, 942 (2017)
54. S. Borisenko, D. Evtushinsky, Q. Gibson, A. Yaresko, T. Kim, M. N. Ali, B. Buechner, M. Hoesch, and R. J. Cava, Time-reversal symmetry breaking type-II Weyl state in YbMnBi_2 , arXiv: 1507.04847 (2015)
55. M. Hirschberger, S. Kushwaha, Z. Wang, Q. Gibson, S. Liang, C. Belvin, B. A. Bernevig, R. J. Cava, and N. P. Ong, The chiral anomaly and thermopower of Weyl fermions in the half-Heusler GdPtBi , *Nat. Mater.* 15, 1161 (2016)
56. C. Felser and B. Yan, Weyl semimetals: Magnetically induced, *Nat. Mater.* 15, 1149 (2016)
57. C. Shekhar, *et al.*, Anomalous Hall effect in Weyl semimetal half-Heusler compounds $R\text{PtBi}$ ($R = \text{Gd}$ and Nd), *Proc. Natl. Acad. Sci. USA* 115, 9140 (2018)
58. S.-Q. Shen, Topological Insulators, 2nd Ed., Springer-Verlag, Berlin Heidelberg, 2017
59. R. Okugawa and S. Murakami, Dispersion of Fermi arcs in Weyl semimetals and their evolutions to Dirac cones, *Phys. Rev. B* 89, 235315 (2014)
60. H. Z. Lu, S. B. Zhang, and S. Q. Shen, High-field magnetoconductivity of topological semimetals with short-range potential, *Phys. Rev. B* 92, 045203 (2015)
61. P. E. C. Ashby and J. P. Carbotte, Theory of magnetic oscillations in Weyl semimetals, *Eur. Phys. J. B* 87 (2014)
62. E. V. Gorbar, V. A. Miransky, and I. A. Shovkovy, Chiral anomaly, dimensional reduction, and magnetoresistivity of Weyl and Dirac semimetals, *Phys. Rev. B* 89, 085126 (2014)
63. H. Z. Lu, W. Y. Shan, W. Yao, Q. Niu, and S. Q. Shen, Massive Dirac fermions and spin physics in an ultrathin film of topological insulator, *Phys. Rev. B* 81, 115407 (2010)
64. S. Jeon, B. B. Zhou, A. Gyenis, B. E. Feldman, I. Kimchi, A. C. Potter, Q. D. Gibson, R. J. Cava, A. Vishwanath, and A. Yazdani, Landau quantization and quasiparticle interference in the three-dimensional Dirac semimetal Cd_3As_2 , *Nat. Mater.* 13, 851 (2014)
65. A. A. Burkov, M. D. Hook, and L. Balents, Topological nodal semimetals, *Phys. Rev. B* 84, 235126 (2011)
66. C.-K. Chiu and A. P. Schnyder, Classification of reflection-symmetry-protected topological semimetals and nodal superconductors, *Phys. Rev. B* 90, 205136 (2014)
67. C. Fang, H. Weng, X. Dai, and Z. Fang, Topological nodal line semimetals, *Chin. Phys. B* 25, 117106 (2016)
68. B.-J. Yang, T. A. Bojesen, T. Morimoto, and A. Furusaki, Topological semimetals protected by off-centered symmetries in nonsymmorphic crystals, *Phys. Rev. B* 95, 075135 (2017)
69. Y. Chen, Y. Xie, S. A. Yang, H. Pan, F. Zhang, M. L. Cohen, and S. Zhang, Nanostructured carbon allotropes with Weyl-like loops and points, *Nano Lett.* 15, 6974 (2015)
70. T. Bzdušek, Q. Wu, A. Rüegg, M. Sigrist, and A. A. Soluyanov, Nodal-chain metals, *Nature* 538, 75 (2016)
71. X. Feng, C. Yue, Z. Song, Q. Wu, and B. Wen, Topological Dirac nodal-net fermions in AlB_2 -type TiB_2 and ZrB_2 , *Phys. Rev. Mater.* 2, 014202 (2018)
72. C.-J. Yi, *et al.*, Observation of a nodal chain with Dirac surface states in TiB_2 , *Phys. Rev. B* 97, 201107 (2018)
73. W. Chen, K. Luo, L. Li, and O. Zilberberg, Proposal for detecting nodal-line semimetal surface states with resonant spin-flipped reflection, *Phys. Rev. Lett.* 121, 166802 (2018)
74. Z. Zhu, *et al.*, Quasiparticle interference and nonsymmorphic effect on a floating band surface state of ZrSiSe , *Nat. Commun.* 9, 4153 (2018)
75. W. Chen and J. L. Lado, Interaction driven surface Chern insulator in nodal line semimetals, arXiv: 1807.06916 (2018)
76. H. Weng, Y. Liang, Q. Xu, R. Yu, Z. Fang, X. Dai, and Y. Kawazoe, Topological node-line semimetal in three-dimensional graphene networks, *Phys. Rev. B* 92, 045108 (2015)
77. R. Yu, H. Weng, Z. Fang, X. Dai, and X. Hu, Topological node-line semimetal and Dirac semimetal state in antiperovskite Cu_3PdN , *Phys. Rev. Lett.* 115, 036807 (2015)
78. Y. Kim, B. J. Wieder, C. L. Kane, and A. M. Rappe, Dirac line nodes in inversion-symmetric crystals, *Phys. Rev. Lett.* 115, 036806 (2015)
79. C. Fang, Y. Chen, H.-Y. Kee, and L. Fu, Topological nodal line semimetals with and without spin-orbital coupling, *Phys. Rev. B* 92, 081201 (2015)
80. Y. Chen, Y.-M. Lu, and H.-Y. Kee, Topological crystalline metal in orthorhombic perovskite iridates, *Nat. Commun.* 6, 6593 (2015)
81. G. Bian, *et al.*, Drumhead surface states and topological nodal-line fermions in TlTaSe_2 , *Phys. Rev. B* 93, 121113 (2016)
82. L. S. Xie, L. M. Schoop, E. M. Seibel, Q. D. Gibson, W. Xie, and R. J. Cava, A new form of Ca_3P_2 with a ring of Dirac nodes, *APL Mater.* 3, 083602 (2015)
83. Y.-H. Chan, C.-K. Chiu, M. Y. Chou, and A. P. Schnyder, Ca_3P_2 and other topological semimetals with line nodes and drumhead surface states, *Phys. Rev. B* 93, 205132 (2016)
84. Y. Du, F. Tang, D. Wang, L. Sheng, E.-j. Kan, C.-G. Duan, S. Y. Savrasov, and X. Wan, CaTe: A new topological node-line and Dirac semimetal, *npj Quantum Mater.* 2, 3 (2017)

85. J. Zhao, R. Yu, H. Weng, and Z. Fang, Topological node-line semimetal in compressed black phosphorus, *Phys. Rev. B* 94, 195104 (2016)
86. A. Yamakage, Y. Yamakawa, Y. Tanaka, and Y. Okamoto, Line-node Dirac semimetal and topological insulating phase in noncentrosymmetric pnictides $\text{CaAg}X$ ($X = \text{P}, \text{As}$), *J. Phys. Soc. Japan* 85, 013708 (2015)
87. Q. Xu, R. Yu, Z. Fang, X. Dai, and H. Weng, Topological nodal line semimetals in the CaP_3 family of materials, *Phys. Rev. B* 95, 045136 (2017)
88. Y.-J. Jin, R. Wang, J.-Z. Zhao, Y.-P. Du, C.-D. Zheng, L.-Y. Gan, J.-F. Liu, H. Xu, and S. Tong, The prediction of a family group of two-dimensional node-line semimetals, *Nanoscale* 9, 13112 (2017)
89. Z. Zhu, M. Li, and J. Li, Topological semimetal to insulator quantum phase transition in the Zintl compounds Ba_2X ($X = \text{Si}, \text{Ge}$), *Phys. Rev. B* 94, 155121 (2016)
90. Q.-F. Liang, J. Zhou, R. Yu, Z. Wang, and H. Weng, Node-surface and node-line fermions from nonsymmorphic lattice symmetries, *Phys. Rev. B* 93, 085427 (2016)
91. M. Zeng, C. Fang, G. Chang, Y.-A. Chen, T. Hsieh, A. Bansil, H. Lin, and L. Fu, Topological semimetals and topological insulators in rare earth monopnictides, arXiv: 1504.03492 (2015)
92. M. Hirayama, R. Okugawa, T. Miyake, and S. Murakami, Topological Dirac nodal lines and surface charges in fcc alkaline earth metals, *Nat Commun.* 8, 14022 (2017)
93. H. Huang, J. Liu, D. Vanderbilt, and W. Duan, Topological nodal-line semimetals in alkaline-earth stannides, germanides, and silicides, *Phys. Rev. B* 93, 201114 (2016)
94. R. Li, H. Ma, X. Cheng, S. Wang, D. Li, Z. Zhang, Y. Li, and X.-Q. Chen, Dirac node lines in pure alkali earth metals, *Phys. Rev. Lett.* 117, 096401 (2016)
95. J.-T. Wang, H. Weng, S. Nie, Z. Fang, Y. Kawazoe, and C. Chen, Body-centered orthorhombic C_{16} : A novel topological node-line semimetal, *Phys. Rev. Lett.* 116, 195501 (2016)
96. Y. Sun, Y. Zhang, C.-X. Liu, C. Felser, and B. Yan, Dirac nodal lines and induced spin Hall effect in metallic rutile oxides, *Phys. Rev. B* 95, 235104 (2017)
97. L. M. Schoop, M. N. Ali, C. Straßer, A. Topp, A. Varykhalov, D. Marchenko, V. Duppel, S. S. P. Parkin, B. V. Lotsch, and C. R. Ast, Dirac cone protected by non-symmorphic symmetry and three-dimensional Dirac line node in ZrSiS , *Nat. Commun.* 7, 11696 (2016)
98. M. Neupane, et al., Observation of topological nodal fermion semimetal phase in ZrSiS , *Phys. Rev. B* 93, 201104 (2016)
99. C. Chen, et al., Dirac line nodes and effect of spin-orbit coupling in the nonsymmorphic critical semimetals $MSiS$ ($M = \text{Hf}, \text{Zr}$), *Phys. Rev. B* 95, 125126 (2017)
100. G. Bian, et al., Topological nodal-line fermions in spin-orbit metal PbTaSe_2 , *Nat. Commun.* 7, 10556 (2016)
101. T.-R. Chang, et al., Topological Dirac surface states and superconducting pairing correlations in PbTaSe_2 , *Phys. Rev. B* 93, 245130 (2016)
102. S. A. Ekahana, et al., Observation of nodal line in non-symmorphic topological semimetal InBi , *New J. Phys.* 19, 065007 (2017)
103. Y. Wu, L.-L. Wang, E. Mun, D. D. Johnson, D. Mou, L. Huang, Y. Lee, S. L. Bud'ko, P. C. Canfield, and A. Kaminski, Dirac node arcs in PtSn_4 , *Nat. Phys.* 12, 667 (2016)
104. A. Alexandradinata and L. Glazman, Semiclassical theory of Landau levels and magnetic breakdown in topological metals, *Phys. Rev. B* 97, 144422 (2018)
105. H. Zhang, C.-X. Liu, X.-L. Qi, X. Dai, Z. Fang, and S.-C. Zhang, Topological insulators in Bi_2Se_3 , Bi_2Te_3 and Sb_2Te_3 with a single Dirac cone on the surface, *Nat. Phys.* 5, 438 (2009)
106. I. A. Nechaev and E. E. Krasovskii, Relativistic $k \cdot p$ Hamiltonians for centrosymmetric topological insulators from *ab initio* wave functions, *Phys. Rev. B* 94, 201410 (2016)
107. W.-Y. Shan, H.-Z. Lu, and S.-Q. Shen, Effective continuous model for surface states and thin films of three-dimensional topological insulators, *New J. Phys.* 12, 043048 (2010)
108. Y. Zhang, et al., Crossover of the three-dimensional topological insulator Bi_2Se_3 to the two-dimensional limit, *Nat. Phys.* 6, 584 (2010)
109. J. Wang, et al., Anomalous anisotropic magnetoresistance in topological insulator films, *Nano Res.* 5, 739 (2012)
110. H. T. He, H. C. Liu, B. K. Li, X. Guo, Z. J. Xu, M. H. Xie, and J. N. Wang, Disorder-induced linear magnetoresistance in (221) topological insulator Bi_2Se_3 films, *Appl. Phys. Lett.* 103, 031606 (2013)
111. S. Wiedmann, et al., Anisotropic and strong negative magnetoresistance in the three-dimensional topological insulator Bi_2Se_3 , *Phys. Rev. B* 94, 081302 (2016)
112. L.-X. Wang, Y. Yan, L. Zhang, Z.-M. Liao, H.-C. Wu, and D.-P. Yu, Zeeman effect on surface electron transport in topological insulator Bi_2Se_3 nanoribbons, *Nanoscale* 7, 16687 (2015)
113. S. L. Adler, Axial-vector vertex in spinor electrodynamics, *Phys. Rev.* 177, 2426 (1969)
114. J. S. Bell and R. Jackiw, A PCAC puzzle: $\pi^0 \rightarrow \gamma\gamma$ in the σ -model, *Il Nuovo Cimento A* 60, 47 (1969)
115. H. B. Nielsen and M. Ninomiya, Absence of neutrinos on a lattice (i): Proof by homotopy theory, *Nucl. Phys. B* 185, 20 (1981)
116. H. J. Kim, K. S. Kim, J. F. Wang, M. Sasaki, N. Satoh, A. Ohnishi, M. Kitaura, M. Yang, and L. Li, Dirac versus Weyl fermions in topological insulators: Adler-Bell-Jackiw anomaly in transport phenomena, *Phys. Rev. Lett.* 111, 246603 (2013)
117. K.-S. Kim, H.-J. Kim, and M. Sasaki, Boltzmann equation approach to anomalous transport in a Weyl metal, *Phys. Rev. B* 89, 195137 (2014)
118. Q. Li, D. E. Kharzeev, C. Zhang, Y. Huang, I. Pletikosic, A. V. Fedorov, R. D. Zhong, J. A. Schneeloch, G. D. Gu, and T. Valla, Chiral magnetic effect in ZrTe_5 , *Nat. Phys.* 12, 550 (2016)

119. J. Xiong, S. K. Kushwaha, T. Liang, J. W. Krizan, M. Hirschberger, W. Wang, R. J. Cava, and N. P. Ong, Evidence for the chiral anomaly in the Dirac semimetal Na₃Bi, *Science* 350, 413 (2015)
120. F. Arnold, *et al.*, Negative magnetoresistance without well-defined chirality in the Weyl semimetal TaP, *Nat. Commun.* 7, 11615 (2016)
121. X. J. Yang, Y. P. Liu, Z. Wang, Y. Zheng, and Z. A. Xu, Chiral anomaly induced negative magnetoresistance in topological Weyl semimetal NbAs, arXiv: 1506.03190 (2015)
122. X. Yang, Y. Li, Z. Wang, Y. Zhen, and Z.-A. Xu, Observation of negative magnetoresistance and nontrivial π Berry's phase in 3D Weyl semi-metal NbAs, arXiv: 1506.02283 (2015)
123. H. Wang, *et al.*, Chiral anomaly and ultrahigh mobility in crystalline HfTe₅, *Phys. Rev. B* 93, 165127 (2016)
124. O. Breunig, Z. Wang, A. A. Taskin, J. Lux, A. Rosch, and Y. Ando, Gigantic negative magnetoresistance in the bulk of a disordered topological insulator, *Nat. Commun.* 8, 15545 (2017)
125. B. A. Assaf, *et al.*, Negative longitudinal magnetoresistance from the anomalous $N = 0$ Landau level in topological materials, *Phys. Rev. Lett.* 119, 106602 (2017)
126. M. Zhang, *et al.*, Topological phase transition-induced triaxial vector magnetoresistance in (Bi_{1-x}In_x)₂Se₃ nanodevices, *ACS Nano* 12, 1537 (2018)
127. C. Fleckenstein, N. Traverso Ziani, and B. Trauzettel, Chiral anomaly in real space from stable fractional charges at the edge of a quantum spin hall insulator, *Phys. Rev. B* 94, 241406 (2016)
128. A. Wolos, *et al.*, *g*-factors of conduction electrons and holes in Bi₂Se₃ three-dimensional topological insulator, *Phys. Rev. B* 93, 155114 (2016)
129. D. Culcer, Transport in three-dimensional topological insulators: Theory and experiment, *Physica E* 44, 860 (2012)
130. G. Sundaram and Q. Niu, Wave-packet dynamics in slowly perturbed crystals: Gradient corrections and Berry-phase effects, *Phys. Rev. B* 59, 14915 (1999)
131. D. Xiao, M. C. Chang, and Q. Niu, Berry phase effects on electronic properties, *Rev. Mod. Phys.* 82, 1959 (2010)
132. G. D. Mahan, Many-Particle Physics, Plenum Press, 1990
133. D. T. Son and B. Z. Spivak, Chiral anomaly and classical negative magnetoresistance of Weyl metals, *Phys. Rev. B* 88, 104412 (2013)
134. S.-K. Yip, Kinetic equation and magneto-conductance for Weyl metal in the clean limit, arXiv: 1508.01010 (2015)
135. A. A. Burkov, Chiral anomaly and diffusive magnetotransport in Weyl metals, *Phys. Rev. Lett.* 113, 247203 (2014)
136. S. Mao, A. Yamakage, and Y. Kuramoto, Tight-binding model for topological insulators: Analysis of helical surface modes over the whole Brillouin zone, *Phys. Rev. B* 84, 115413 (2011)
137. J. G. Checkelsky, Y. S. Hor, M.-H. Liu, D.-X. Qu, R. J. Cava, and N. P. Ong, Quantum interference in macroscopic crystals of nonmetallic Bi₂Se₃, *Phys. Rev. Lett.* 103, 246601 (2009)
138. J. Chen, *et al.*, Gate-voltage control of chemical potential and weak antilocalization in Bi₂Se₃, *Phys. Rev. Lett.* 105, 176602 (2010)
139. J. Wang, A. M. DaSilva, C.-Z. Chang, K. He, J. K. Jain, N. Samarth, X.-C. Ma, Q.-K. Xue, and M. H. W. Chan, Evidence for electron-electron interaction in topological insulator thin films, *Phys. Rev. B* 83, 245438 (2011)
140. H.-T. He, G. Wang, T. Zhang, I.-K. Sou, G. K. L. Wong, J.-N. Wang, H.-Z. Lu, S.-Q. Shen, and F.-C. Zhang, Impurity effect on weak antilocalization in the topological insulator Bi₂Te₃, *Phys. Rev. Lett.* 106, 166805 (2011)
141. H. Köhler and E. Wöchner, The *g*-factor of the conduction electrons in Bi₂Se₃, *physica status solidi (b)* 67, 665 (1975)
142. A. Srinivasan, K. L. Hudson, D. Miserev, L. A. Yeoh, O. Klochan, K. Muraki, Y. Hirayama, O. P. Sushkov, and A. R. Hamilton, Electrical control of the sign of the *g* factor in a GaAs hole quantum point contact, *Phys. Rev. B* 94, 041406 (2016)
143. T. Morimoto, S. Zhong, J. Orenstein, and J. E. Moore, Semiclassical theory of nonlinear magneto-optical responses with applications to topological Dirac/Weyl semimetals, *Phys. Rev. B* 94, 245121 (2016)
144. Y. Gao, S. A. Yang, and Q. Niu, Intrinsic relative magnetocconductivity of nonmagnetic metals, *Phys. Rev. B* 95, 165135 (2017)
145. Y. Gao, S. A. Yang, and Q. Niu, Field induced positional shift of Bloch electrons and its dynamical implications, *Phys. Rev. Lett.* 112, 166601 (2014)
146. Y. Gao, S. A. Yang, and Q. Niu, Geometrical effects in orbital magnetic susceptibility, *Phys. Rev. B* 91, 214405 (2015)
147. P. Goswami, J. H. Pixley, and S. Das Sarma, Axial anomaly and longitudinal magnetoresistance of a generic three-dimensional metal, *Phys. Rev. B* 92, 075205 (2015)
148. R. D. dos Reis, M. O. Ajesh, N. Kumar, F. Arnold, C. Shekhar, M. Naumann, M. Schmidt, M. Nicklas, and E. Hassinger, On the search for the chiral anomaly in Weyl semimetals: the negative longitudinal magnetoresistance, *New J. Phys.* 18, 085006 (2016)
149. A. V. Andreev and B. Z. Spivak, Longitudinal negative magnetoresistance and magnetotransport phenomena in conventional and topological conductors, *Phys. Rev. Lett.* 120, 026601 (2018)
150. H. Ishizuka and N. Nagaosa, Robustness of anomaly-related magnetoresistance in doped Weyl semimetals, arXiv: 1808.09093 (2018)
151. D. Shoenberg, Magnetic Oscillations in Metals, Cambridge University Press, 1984
152. G. P. Mikitik and Y. V. Sharlai, Manifestation of Berry's phase in metal physics, *Phys. Rev. Lett.* 82, 2147 (1999)

153. I. M. Lifshitz and A. M. Kosevich, Theory of magnetic susceptibility in metals at low temperatures, *Sov. Phys. JETP* 2, 636 (1956)
154. D. Shoenberg, The Fermi surfaces of copper, silver and gold. I. the de Haas–van Alphen effect, *Phil. Trans. R. Soc. Lond. A* 255, 85 (1962)
155. P. T. Coleridge and I. M. Templeton, High precision de Haas–van Alphen measurements in the noble metals, *J. Phys. F: Metal Phys.* 2, 643 (1972)
156. I. A. Luk'yanchuk and Y. Kopelevich, Phase analysis of quantum oscillations in graphite, *Phys. Rev. Lett.* 93, 166402 (2004)
157. G. E. Volovik, The Universe in a Helium Droplet, Clarendon Press, Oxford, 2003
158. Y. Zhang, Y.-W. Tan, H. L. Stormer, and P. Kim, Experimental observation of the quantum Hall effect and Berry's phase in graphene, *Nature* 438, 201 (2005)
159. H. Murakawa, M. S. Bahramy, M. Tokunaga, Y. Kohama, C. Bell, Y. Kaneko, N. Nagaosa, H. Y. Hwang, and Y. Tokura, Detection of Berry's phase in a bulk Rashba semiconductor, *Science* 342, 1490 (2013)
160. L. P. He, X. C. Hong, J. K. Dong, J. Pan, Z. Zhang, J. Zhang, and S. Y. Li, Quantum transport evidence for the three-dimensional Dirac semimetal phase in Cd₃As₂, *Phys. Rev. Lett.* 113, 246402 (2014)
161. M. Novak, S. Sasaki, K. Segawa, and Y. Ando, Large linear magnetoresistance in the Dirac semimetal TlBiSSe, *Phys. Rev. B* 91, 041203(R) (2015)
162. Y. F. Zhao, *et al.*, Anisotropic Fermi surface and quantum limit transport in high mobility three-dimensional Dirac semimetal Cd₃As₂, *Phys. Rev. X* 5, 031037 (2015)
163. J. Du, *et al.*, Large unsaturated positive and negative magnetoresistance in Weyl semimetal TaP, *Sci. China-Phys. Mech. Astron.* 59, 657406 (2016)
164. Z. Wang, *et al.*, Helicity-protected ultrahigh mobility Weyl fermions in NbP, *Phys. Rev. B* 93, 121112(R) (2016)
165. J. Cao, *et al.*, Landau level splitting in Cd₃As₂ under high magnetic fields, *Nat. Commun.* 6, 7779 (2015)
166. C. Zhang, Z. Yuan, S. Xu, Z. Lin, B. Tong, M. Z. Hasan, J. Wang, C. Zhang, and S. Jia, Tantalum monoarsenide: an exotic compensated semimetal, arXiv: 1502.00251 (2015)
167. A. Narayanan, *et al.*, Linear magnetoresistance caused by mobility fluctuations in *n*-doped Cd₃As₂, *Phys. Rev. Lett.* 114, 117201 (2015)
168. J. Park, *et al.*, Anisotropic Dirac Fermions in a Bi square net of SrMnBi₂, *Phys. Rev. Lett.* 107, 126402 (2011)
169. F.-X. Xiang, X.-L. Wang, M. Veldhorst, S.-X. Dou, and M. S. Fuhrer, Observation of topological transition of Fermi surface from a spindle torus to a torus in bulk Rashba spin-split BiTeCl, *Phys. Rev. B* 92, 035123 (2015)
170. F. F. Tafti, Q. D. Gibson, S. K. Kushwaha, N. Halldoraachchige, and R. J. Cava, Resistivity plateau and extreme magnetoresistance in LaSb, *Nat. Phys.* 12, 272 (2016)
171. Y. Luo, N. J. Ghimire, M. Wartenbe, H. Choi, M. Neupane, R. D. McDonald, E. D. Bauer, J. Zhu, J. D. Thompson, and F. Ronning, Electron–hole compensation effect between topologically trivial electrons and nontrivial holes in NbAs, *Phys. Rev. B* 92, 205134 (2015)
172. F. Arnold, M. Naumann, S.-C. Wu, Y. Sun, M. Schmidt, H. Borrmann, C. Felser, B. Yan, and E. Hassinger, Chiral Weyl pockets and Fermi surface topology of the Weyl semimetal TaAs, *Phys. Rev. Lett.* 117, 146401 (2016)
173. J. Klotz, *et al.*, Quantum oscillations and the Fermi surface topology of the Weyl semimetal NbP, *Phys. Rev. B* 93, 121105 (2016)
174. R. D. dos Reis, S. C. Wu, Y. Sun, M. O. Ajeesh, C. Shekhar, M. Schmidt, C. Felser, B. Yan, and M. Nicklas, Pressure tuning the Fermi surface topology of the Weyl semimetal NbP, *Phys. Rev. B* 93, 205102 (2016)
175. P. Sergelius, *et al.*, Berry phase and band structure analysis of the Weyl semimetal NbP, *Sci. Rep.* 6, 33859 (2016)
176. N. Kumar, K. Manna, Y. Qi, S.-C. Wu, L. Wang, B. Yan, C. Felser, and C. Shekhar, Unusual magnetotransport from Si-square nets in topological semimetal HfSiS, *Phys. Rev. B* 95, 121109 (2017)
177. R. Singha, A. K. Pariari, B. Satpati, and P. Mandal, Large nonsaturating magnetoresistance and signature of nondegenerate Dirac nodes in ZrSiS, *Proc. Natl. Acad. Sci. USA* 114, 2468 (2017)
178. M. N. Ali, L. M. Schoop, C. Garg, J. M. Lippmann, E. Lara, B. Lotsch, and S. S. P. Parkin, Butterfly magnetoresistance, quasi-2D Dirac Fermi surface and topological phase transition in ZrSiS, *Sci. Adv.* 2, e1601742 (2016)
179. X. Wang, *et al.*, Evidence of both surface and bulk Dirac bands and anisotropic nonsaturating magnetoresistance in ZrSiS, *Adv. Electron. Mater.* 2, 1600228 (2016)
180. Y.-Y. Lv, B.-B. Zhang, X. Li, S.-H. Yao, Y. B. Chen, J. Zhou, S.-T. Zhang, M.-H. Lu, and Y.-F. Chen, Extremely large and significantly anisotropic magnetoresistance in ZrSiS single crystals, *App. Phys. Lett.* 108, 244101 (2016)
181. J. Hu, Z. Tang, J. Liu, Y. Zhu, J. Wei, and Z. Mao, Nearly massless Dirac fermions and strong Zeeman splitting in the nodal-line semimetal ZrSiS probed by de Haas–van Alphen quantum oscillations, *Phys. Rev. B* 96, 045127 (2017)
182. H. Pan, *et al.*, Three-dimensional anisotropic magnetoresistance in the Dirac node-line material ZrSiSe, *Sci. Rep.* 8, 9340 (2018)
183. J. Hu, *et al.*, Evidence of topological nodal-line fermions in ZrSiSe and ZrSiTe, *Phys. Rev. Lett.* 117, 016602 (2016)
184. J. Hu, Y. L. Zhu, D. Graf, Z. J. Tang, J. Y. Liu, and Z. Q. Mao, Quantum oscillation studies of the topological semimetal candidate ZrGeM (*M*=S, Se, Te), *Phys. Rev. B* 95, 205134 (2017)
185. M. Charbonneau, K. M. van Vliet, and P. Vasilopoulos, Linear response theory revisited III: One-body response formulas and generalized Boltzmann equations, *J. Math. Phys.* 23, 318 (1982)

186. P. Vasilopoulos and C. Van Vliet, Linear response theory revisited (IV): Applications, *J. Math. Phys.* 25, 1391 (1984)
187. C. M. Wang and X. L. Lei, Linear magnetoresistance on the topological surface, *Phys. Rev. B* 86, 035442 (2012)
188. C. M. Wang and X. L. Lei, Linear magnetotransport in monolayer MoS₂, *Phys. Rev. B* 92, 125303 (2015)
189. D.-X. Qu, Y. S. Hor, J. Xiong, R. J. Cava, and N. P. Ong, Quantum oscillations and hall anomaly of surface states in the topological insulator Bi₂Te₃, *Science* 329, 821 (2010)
190. S. Datta, *Electronic Transport in Mesoscopic Systems*, Cambridge University Press, 1997
191. F. T. Vasko and O. E. Raichev, *Quantum Kinetic Theory and Applications: Electrons, Photons, Phonons*, Springer Science & Business Media, 2006
192. A. A. Abrikosov, Quantum magnetoresistance, *Phys. Rev. B* 58, 2788 (1998)
193. J. Xiong, S. Kushwaha, J. Krizan, T. Liang, R. J. Cava, and N. P. Ong, Anomalous conductivity tensor in the Dirac semimetal Na₃Bi, *EPL* 114, 27002 (2016)
194. J. Hu, *et al.*, π Berry phase and Zeeman splitting of TaP probed by high field magnetotransport measurements, *Sci. Rep.* 6, 18674 (2016)
195. L. Onsager, Interpretation of the de Haas–van Alphen effect, *Philos. Mag.* 43, 1006 (1952)
196. M. Phillips and V. Aji, Tunable line node semimetals, *Phys. Rev. B* 90, 115111 (2014)
197. W. Chen, H.-Z. Lu, and O. Zilberberg, Weak localization and antilocalization in nodal-line semimetals: Dimensionality and topological effects, arXiv: 1902.06921 (2019)
198. K. v. Klitzing, G. Dorda, and M. Pepper, New method for high-accuracy determination of the fine-structure constant based on quantized Hall resistance, *Phys. Rev. Lett.* 45, 494 (1980)
199. D. J. Thouless, M. Kohmoto, M. P. Nightingale, and M. den Nijs, Quantized Hall conductance in a two-dimensional periodic potential, *Phys. Rev. Lett.* 49, 405 (1982)
200. K. S. Novoselov, A. K. Geim, S. V. Morozov, D. Jiang, M. I. Katsnelson, I. V. Grigorieva, S. V. Dubonos, and A. A. Firsov, Two-dimensional gas of massless Dirac fermions in graphene, *Nature* 438, 197 (2005)
201. Y. Xu, I. Miotkowski, C. Liu, J. Tian, H. Nam, N. Ali-doust, J. Hu, C.-K. Shih, M. Z. Hasan, and Y. P. Chen, Observation of topological surface state quantum Hall effect in an intrinsic three-dimensional topological insulator, *Nat. Phys.* 10, 956 (2014)
202. R. Yoshimi, K. Yasuda, A. Tsukazaki, K. S. Takahashi, N. Nagaosa, M. Kawasaki, and Y. Tokura, Quantum Hall states stabilized in semi-magnetic bilayers of topological insulators, *Nat. Commun.* 6, 8530 (2015)
203. M. Brahlek, N. Bansal, N. Koirala, S. Y. Xu, M. Neupane, C. Liu, M. Z. Hasan, and S. Oh, Topological-metal to band-insulator transition in (Bi_{1-x}In_x)₂Se₃ thin films, *Phys. Rev. Lett.* 109, 186403 (2012)
204. L. Wu, M. Brahlek, R. Valdes Aquilar, A. V. Stier, C. M. Morris, Y. Lubashevsky, L. S. Bilbro, N. Bansal, S. Oh, and N. P. Armitage, A sudden collapse in the transport lifetime across the topological phase transition in (Bi_{1-x}In_x)₂Se₃, *Nat. Phys.* 9, 410 (2013)
205. P. Hosur, Friedel oscillations due to Fermi arcs in Weyl semimetals, *Phys. Rev. B* 86, 195102 (2012)
206. Y. Baum, E. Berg, S. A. Parameswaran, and A. Stern, Current at a distance and resonant transparency in Weyl semimetals, *Phys. Rev. X* 5, 041046 (2015)
207. E. V. Gorbar, V. A. Miransky, I. A. Shovkovy, and P. O. Sukhachov, Origin of dissipative Fermi arc transport in Weyl semimetals, *Phys. Rev. B* 93, 235127 (2016)
208. Y. Ominato and M. Koshino, Magnetotransport in Weyl semimetals in the quantum limit: Role of topological surface states, *Phys. Rev. B* 93, 245304 (2016)
209. T. M. McCormick, S. J. Watzman, J. P. Heremans, and N. Trivedi, Fermi arc mediated entropy transport in topological semimetals, *Phys. Rev. B* 97, 195152 (2018)
210. C. Shekhar, *et al.*, Extremely large magnetoresistance and ultrahigh mobility in the topological Weyl semimetal NbP, *Nat. Phys.* 11, 645 (2015)
211. T. Liang, Q. Gibson, M. N. Ali, M. H. Liu, R. J. Cava, and N. P. Ong, Ultrahigh mobility and giant magnetoresistance in the Dirac semimetal Cd₃As₂, *Nat. Mater.* 14, 280 (2015)
212. P. J. W. Moll, N. L. Nair, T. Helm, A. C. Potter, I. Kimchi, A. Vishwanath, and J. G. Analytis, Transport evidence for Fermi-arc-mediated chirality transfer in the Dirac semimetal Cd₃As₂, *Nature* 535, 266 (2016)
213. G. Rosenberg, H.-M. Guo, and M. Franz, Wormhole effect in a strong topological insulator, *Phys. Rev. B* 82, 041104 (2010)
214. J. Ruan, S.-K. Jian, H. Yao, H. Zhang, S.-C. Zhang, and D. Xing, Symmetry-protected ideal Weyl semimetal in HgTe-class materials, *Nat. Commun.* 7, 11136 (2016)
215. A. C. Potter, I. Kimchi, and A. Vishwanath, Quantum oscillations from surface Fermi arcs in Weyl and Dirac semimetals, *Nat. Commun.* 5, 5161 (2014)
216. M. Uchida, *et al.*, Quantum Hall effect in Cd₃As₂ films, APS March Meeting A44.00005 (2017)
217. M. Uchida, *et al.*, Quantum Hall states observed in thin films of Dirac semimetal Cd₃As₂, *Nat. Commun.* 8, 2274 (2017)
218. T. Schumann, L. Galletti, D. A. Kealhofer, H. Kim, M. Goyal, and S. Stemmer, Observation of the quantum Hall effect in confined films of the three-dimensional Dirac semimetal Cd₃As₂, *Phys. Rev. Lett.* 120, 016801 (2018)
219. C. Zhang, *et al.*, Quantum Hall effect based on Weyl orbit in Cd₃As₂, *Nature* 565, 331 (2019)
220. V. P. Gusynin and S. G. Sharapov, Unconventional integer quantum Hall effect in graphene, *Phys. Rev. Lett.* 95, 146801 (2005)
221. A. A. Zyuzin and A. A. Burkov, Thin topological insulator film in a perpendicular magnetic field, *Phys. Rev. B* 83, 195413 (2011)

222. S. B. Zhang, Y. Y. Zhang, and S. Q. Shen, Robustness of quantum spin Hall effect in an external magnetic field, *Phys. Rev. B* 90, 115305 (2014)
223. S. B. Zhang, H. Z. Lu, and S. Q. Shen, Edge states and integer quantum Hall effect in topological insulator thin films, *Sci. Rep.* 5, 13277 (2015)
224. A. Pertsova, C. M. Canali, and A. H. MacDonald, Quantum Hall edge states in topological insulator nanoribbons, *Phys. Rev. B* 94, 121409 (2016)
225. H. Zheng, *et al.*, Atomic-scale visualization of quantum interference on a Weyl semimetal surface by scanning tunneling microscopy, *ACS Nano* 10, 1378 (2016)
226. E. Y. Ma, *et al.*, Unexpected edge conduction in mercury telluride quantum wells under broken time-reversal symmetry, *Nat. Commun.* 6, 7252 (2015)
227. M. Kargarian, M. Randeria, and Y.-M. Lu, Are the surface Fermi arcs in Dirac semimetals topologically protected? *Proc. Natl. Acad. Sci. USA* 113, 8648 (2016)
228. J. Cano, B. Bradlyn, Z. Wang, M. Hirschberger, N. P. Ong, and B. A. Bernevig, Chiral anomaly factory: Creating Weyl fermions with a magnetic field, *Phys. Rev. B* 95, 161306 (2017)
229. S. Q. Shen, M. Ma, X. C. Xie, and F. C. Zhang, Resonant spin Hall conductance in two-dimensional electron systems with a Rashba interaction in a perpendicular magnetic field, *Phys. Rev. Lett.* 92, 256603 (2004)
230. M. Z. Hasan and C. L. Kane, Colloquium: Topological insulators, *Rev. Mod. Phys.* 82, 3045 (2010)
231. X.-L. Qi and S.-C. Zhang, Topological insulators and superconductors, *Rev. Mod. Phys.* 83, 1057 (2011)
232. R. Yu, W. Zhang, H.-J. Zhang, S.-C. Zhang, X. Dai, and Z. Fang, Quantized anomalous Hall effect in magnetic topological insulators, *Science* 329, 61 (2010)
233. C.-Z. Chang, *et al.*, Experimental observation of the quantum anomalous Hall effect in a magnetic topological insulator, *Science* 340, 167 (2013)
234. L. Fu and C. L. Kane, Superconducting proximity effect and Majorana fermions at the surface of a topological insulator, *Phys. Rev. Lett.* 100, 096407 (2008)
235. A. R. Akhmerov, J. Nilsson, and C. W. J. Beenakker, Electrically detected interferometry of Majorana fermions in a topological insulator, *Phys. Rev. Lett.* 102, 216404 (2009)
236. I. Belopolski, *et al.*, A novel artificial condensed matter lattice and a new platform for one-dimensional topological phases, *Sci. Adv.* 3, 3 (2017)
237. C.-K. Chiu, G. Bian, H. Zheng, J.-X. Yin, S. S. Zhang, D. S. Sanchez, I. Belopolski, S.-Y. Xu, and M. Z. Hasan, Chiral majorana fermion modes on the surface of superconducting topological insulators, *EPL* 123, 47005 (2018)
238. M. König, S. Wiedmann, C. Brüne, A. Roth, H. Buhmann, L. W. Molenkamp, X.-L. Qi, and S.-C. Zhang, Quantum spin Hall insulator state in HgTe quantum wells, *Science* 318, 766 (2007)
239. B. Büttner, *et al.*, Single valley Dirac fermions in zero-gap HgTe quantum wells, *Nat. Phys.* 7, 418 (2011)
240. A. Mani and C. Benjamin, Probing helicity and the topological origins of helicity via non-local Hanbury–Brown and Twiss correlations, *Sci. Rep.* 7, 6954 (2017)
241. H. Weng, X. Dai, and Z. Fang, Transition-metal pentatelluride $ZrTe_5$ and $HfTe_5$: A paradigm for large-gap quantum spin Hall insulators, *Phys. Rev. X* 4, 011002 (2014)
242. Y. Liu, *et al.*, Zeeman splitting and dynamical mass generation in Dirac semimetal $ZrTe_5$, *Nat. Commun.* 7, 12516 (2016)
243. W. Zhang, R. Yu, W. Feng, Y. Yao, H. Weng, X. Dai, and Z. Fang, Topological aspect and quantum magnetoresistance of $\beta\text{-Ag}_2\text{Te}$, *Phys. Rev. Lett.* 106, 156808 (2011)
244. H.-Z. Lu, J. Shi, and S.-Q. Shen, Competition between weak localization and antilocalization in topological surface states, *Phys. Rev. Lett.* 107, 076801 (2011)
245. H.-W. Wang, B. Fu, and S.-Q. Shen, Intrinsic magnetoresistance in three-dimensional Dirac materials with low carrier density, *Phys. Rev. B* 98, 081202 (2018)
246. A. Alexandradinata and L. Glazman, Geometric phase and orbital moment in quantization rules for magnetic breakdown, *Phys. Rev. Lett.* 119, 256601 (2017)
247. A. Alexandradinata, C. Wang, W. Duan, and L. Glazman, Revealing the topology of fermi-surface wave functions from magnetic quantum oscillations, *Phys. Rev. X* 8, 011027 (2018)
248. J. Höller and A. Alexandradinata, Topological Bloch oscillations, *Phys. Rev. B* 98, 024310 (2018)
249. T. E. O'Brien, M. Diez, and C. W. J. Beenakker, Magnetic breakdown and Klein tunneling in a type-II Weyl semimetal, *Phys. Rev. Lett.* 116, 236401 (2016)
250. F. Fei, *et al.*, Nontrivial berry phase and type-ii dirac transport in the layered material $PdTe_2$, *Phys. Rev. B* 96, 041201 (2017)
251. H. Yang, R. Moessner, and L.-K. Lim, Quantum oscillations in nodal line systems, *Phys. Rev. B* 97, 165118 (2018)
252. L. Oroszlány, B. Dóra, J. Cserti, and A. Cortijo, Topological and trivial magnetic oscillations in nodal loop semimetals, *Phys. Rev. B* 97, 205107 (2018)
253. C. Zhang, *et al.*, Evolution of Weyl orbit and quantum Hall effect in Dirac semimetal Cd_3As_2 , *Nat. Commun.* 8, 1272 (2017)
254. Y. Zhang, D. Bulmash, P. Hosur, A. C. Potter, and A. Vishwanath, Quantum oscillations from generic surface Fermi arcs and bulk chiral modes in Weyl semimetals, *Sci. Rep.* 6, 23741 (2016)
255. B. I. Halperin, Possible states for a three-dimensional electron gas in a strong magnetic field, *Japanese J. Appl. Phys.* 26, 1913 (1987)
256. F. Tang, *et al.*, Three-dimensional quantum Hall effect and metal-insulator transition in $ZrTe_5$, arXiv: 1807.02678 (2018)
257. H.-Z. Lu, Perspective: 3D quantum Hall effect, *Natl. Sci. Rev.*, nwy082 (2018)

258. H. Wang, *et al.*, Discovery of log-periodic oscillations in ultraquantum topological materials, *Sci. Adv.* 4, 11 (2018)
259. H. Wang, *et al.*, Log-periodic quantum magneto-oscillations and discrete scale invariance in topological material HfTe₅, arXiv: 1810.03109 (2018)
260. P. Zhang and H. Zhai, Efimov effect in Dirac semi-metals, *Front. Phys.* 13, 137204 (2018)
261. H. Liu, H. Jiang, Z. Wang, R. Joynt, and X. C. Xie, Discrete scale invariance in topological semimetals, arXiv: 1807.02459 (2018)
262. H. Weng, C. Fang, Z. Fang, and X. Dai, Topological semimetals with triply degenerate nodal points in θ -phase tantalum nitride, *Phys. Rev. B* 93, 241202 (2016)
263. H. Weng, C. Fang, Z. Fang, and X. Dai, Coexistence of Weyl fermion and massless triply degenerate nodal points, *Phys. Rev. B* 94, 165201 (2016)
264. B. Bradlyn, J. Cano, Z. Wang, M. G. Vergniory, C. Felser, R. J. Cava, and B. A. Bernevig, Beyond Dirac and Weyl fermions: Unconventional quasiparticles in conventional crystals, *Science* 353 (2016)
265. G. Chang, *et al.*, Nexus fermions in topological symmorphic crystalline metals, *Sci. Rep.* 7, 1688 (2017)
266. B. Q. Lv, *et al.*, Observation of three-component fermions in the topological semimetal molybdenum phosphide, *Nature* 546, 627 (2017)
267. J.-Z. Ma, *et al.*, Three-component fermions with surface Fermi arcs in tungsten carbide, *Nat. Phys.* 14, 349 (2018)
268. J. B. He, D. Chen, W. L. Zhu, S. Zhang, L. X. Zhao, Z. A. Ren, and G. F. Chen, Magnetotransport properties of the triply degenerate node topological semimetal tungsten carbide, *Phys. Rev. B* 95, 195165 (2017)
269. W. L. Zhu, J. B. He, S. Zhang, D. Chen, L. Shan, Z. A. Ren, and G. F. Chen, Magnetotransport properties of the new-type topological semimetal ZrTe, arXiv: 1707.00942 (2017)
270. C. Shekhar, *et al.*, Extremely high conductivity observed in the unconventional triple point fermion material MoP, arXiv: 1703.03736 (2017)
271. A. K. Nayak, *et al.*, Large anomalous Hall effect driven by a nonvanishing Berry curvature in the noncolinear antiferromagnet Mn₃Ge, *Sci. Adv.* 2, 4 (2016)
272. Z. Wang, M. G. Vergniory, S. Kushwaha, M. Hirschberger, E. V. Chulkov, A. Ernst, N. P. Ong, R. J. Cava, and B. A. Bernevig, Time-reversal-breaking Weyl fermions in magnetic Heusler alloys, *Phys. Rev. Lett.* 117, 236401 (2016)
273. G. Chang, *et al.*, Room-temperature magnetic topological Weyl fermion and nodal line semimetal states in half-metallic Heusler Co₂TiX (X=Si, Ge, or Sn), *Sci. Rep.* 6, 38839 (2016)
274. S. Nie, G. Xu, F. B. Prinz, and S.-C. Zhang, Topological semimetal in honeycomb lattice LnSI, *Proc. Natl. Acad. Sci. USA* 114, 10596 (2017)
275. H. Yang, Y. Sun, Y. Zhang, W.-J. Shi, S. S. P. Parkin, and B. Yan, Topological Weyl semimetals in the chiral antiferromagnetic materials Mn₃Ge and Mn₃Sn, *New J. Phys.* 19, 015008 (2017)
276. E. Liu, *et al.*, Giant anomalous Hall effect in a ferromagnetic kagome-lattice semimetal, *Nat. Phys.* 14, 1125 (2018)
277. Q. Wang, Y. Xu, R. Lou, Z. Liu, M. Li, Y. Huang, D. Shen, H. Weng, S. Wang, and H. Lei, Large intrinsic anomalous Hall effect in half-metallic ferromagnet Co₃Sn₂S₂ with magnetic Weyl fermions, *Nat. Commun.* 9, 3681 (2018)
278. S. N. Guin, *et al.*, Anomalous Nernst effect beyond the magnetization scaling relation in the ferromagnetic Heusler compound Co₂MnGa, arXiv: 1806.06753 (2018)
279. G. Chang, *et al.*, Magnetic and noncentrosymmetric weyl fermion semimetals in the *RAlGe* family of compounds (*R*=rare earth), *Phys. Rev. B* 97, 041104 (2018)
280. J.-X. Yin, *et al.*, Giant and anisotropic many-body spin-orbit tunability in a strongly correlated kagome magnet, *Nature* 562, 91 (2018)
281. S.-M. Huang, *et al.*, New type of Weyl semimetal with quadratic double Weyl fermions, *Proc. Natl. Acad. Sci. USA* 113, 1180 (2016)
282. A. A. Soluyanov, D. Gresch, Z. Wang, Q. Wu, M. Troyer, X. Dai, and B. A. Bernevig, Type-II Weyl semimetals, *Nature* 527, 495 (2015)
283. K. Deng, *et al.*, Experimental observation of topological fermi arcs in type-II Weyl semimetal MoTe₂, *Nat. Phys.* 12, 1105 (2016)
284. J. Jiang, *et al.*, Signature of type-II Weyl semimetal phase in MoTe₂, *Nat. Commun.* 8, 13973 (2017)
285. Y. Wang, *et al.*, Gate-tunable negative longitudinal magnetoresistance in the predicted type-II Weyl semimetal WTe₂, *Nat. Commun.* 7, 13142 (2016)
286. E. Zhang, *et al.*, Tunable positive to negative magnetoresistance in atomically thin WTe₂, *Nano Lett.* 17, 878 (2017)
287. D. Chen, *et al.*, Magnetotransport properties of the type-II Weyl semimetal candidate Ta₃S₂, *Phys. Rev. B* 94, 174411 (2016)
288. S. Khim, *et al.*, Magnetotransport and de Haas-van Alphen measurements in the type-II Weyl semimetal TaIrTe₄, *Phys. Rev. B* 94, 165145 (2016)
289. S.-Y. Xu, *et al.*, Discovery of lorentz-violating type II Weyl fermions in laalge, *Sci. Adv.* 3, 6 (2017)
290. I. Belopolski, *et al.*, Discovery of a new type of topological Weyl fermion semimetal state in Mo_xW_{1-x}Te₂, *Nat. Commun.* 7, 13643 (2016)
291. G. Chang, *et al.*, A strongly robust type II Weyl fermion semimetal state in Ta₃S₂, *Sci. Adv.* 2, 6 (2016)
292. C. Zhong, Y. Chen, Z.-M. Yu, Y. Xie, H. Wang, S. A. Yang, and S. Zhang, Three-dimensional pentagon carbon with a genesis of emergent fermions, *Nat. Commun.* 8, 15641 (2017)

293. W. Chen, H.-Z. Lu, and J.-M. Hou, Topological semimetals with a double-helix nodal link, *Phys. Rev. B* 96, 041102 (2017)
294. Z. Yan, R. Bi, H. Shen, L. Lu, S.-C. Zhang, and Z. Wang, Nodal-link semimetals, *Phys. Rev. B* 96, 041103 (2017)
295. M. Ezawa, Topological semimetals carrying arbitrary Hopf numbers: Fermi surface topologies of a Hopf link, Solomon's knot, trefoil knot, and other linked nodal varieties, *Phys. Rev. B* 96, 041202 (2017)
296. L.-X. Wang, C.-Z. Li, D.-P. Yu, and Z.-M. Liao, Aharonov–Bohm oscillations in Dirac semimetal Cd₃As₂ nanowires, *Nat. Commun.* 7, 10769 (2016)
297. H. Zheng, *et al.*, Atomic-scale visualization of quasiparticle interference on a type-II Weyl semimetal surface, *Phys. Rev. Lett.* 117, 266804 (2016)
298. H. Zheng and M. Z. Hasan, Quasiparticle interference on type-I and type-II Weyl semimetal surfaces: A review, *Advances in Physics: X* 3, 1466661 (2018)
299. H. Zheng, *et al.*, Mirror protected Dirac fermions on a Weyl semimetal NbP surface, *Phys. Rev. Lett.* 119, 196403 (2017)
300. G. Chang, *et al.*, Signatures of Fermi arcs in the quasiparticle interferences of the Weyl semimetals TaAs and NbP, *Phys. Rev. Lett.* 116, 066601 (2016)
301. S. Wang, B.-C. Lin, W.-Z. Zheng, D. Yu, and Z.-M. Liao, Fano interference between bulk and surface states of a Dirac semimetal Cd₃As₂ nanowire, *Phys. Rev. Lett.* 120, 257701 (2018)
302. J. Gooth, *et al.*, Experimental signatures of the mixed axial-gravitational anomaly in the Weyl semimetal NbP, *Nature* 547, 324 (2017)